High winter precipitation in Southern Europe during the Last Glacial Maximum as inferred from pollen sequences

Jena Zumaque, Anne de Vernal, Frédérique Eynaud, Jon Camuera, Gonzalo Jiménez-Moreno, Nathalie Combourieu-Nebout

To cite this version:

Jena Zumaque, Anne de Vernal, Frédérique Eynaud, Jon Camuera, Gonzalo Jiménez-Moreno, et al.. High winter precipitation in Southern Europe during the Last Glacial Maximum as inferred from pollen sequences. Quaternary Science Reviews, 2026, 380, pp.109906. ⟨10.1016/j.quascirev.2026.109906⟩. ⟨hal-05553896⟩

HAL Id: hal-05553896

https://hal.science/hal-05553896v1

Submitted on 3 Apr 2026

Quaternary Science Reviews 380 (2026) 109906

Contents lists available at ScienceDirect

Quaternary Science Reviews

journal homepage: www.elsevier.com/locate/quascirev

High winter precipitation in Southern Europe during the Last Glacial Maximum as inferred from pollen sequences

Jena Zumaque[a,*], Anne de Vernal[a], Frédérique Eynaud[b], Jon Camuera[c], Gonzalo Jiménez-Moreno[d], Nathalie Combourieu-Nebout[e]

[a] *GEOTOP - Centre de recherche sur la dynamique du système Terre, Université du Québec à Montréal, Canada*
[b] *EPOC (Environnements & Paléoenvironnements Océaniques et Continentaux) Laboratory, UMR 5805, Bordeaux University, France*
[c] *Andalusian Earth Sciences Institute (IACT), Spanish National Research Council (CSIC), Armilla, Granada, Spain*
[d] *Department of Stratigraphy and Paleontology, University of Granada, Spain*
[e] *UMR 7194 CNRS, MNHN, HNHP (Histoire Naturelle des Humanités Préhistoriques), Institut de Paléontologie Humaine, Paris, France*

ARTICLE INFO

Handling Editor: Dr Yan Zhao

Keywords:
Last Glacial Maximum
Southern Europe
Pollen records
Modern Analogue Technique
Winter temperatures and precipitation

ABSTRACT

The climate of the Last Glacial Maximum (LGM) in southern Europe has been thoroughly documented. Still, discrepancies exist between the climatic information provided by pollen data, which mainly indicate steppe vegetation and thus arid conditions, and some model simulations that rather suggest large amounts of precipitation, notably in winter. Here, we investigate the regional vegetation and seasonal climate from 28 ka to 10 ka using published pollen sequences from five sites, including core SU81-18 located on the western Iberian Margin, ODP Site 976 in the Alboran Sea, Padul in Southeastern Spain, Lago Grandi di Monticchio (Monticchio) in southern Italy and Xinias in Greece. Pollen-based estimates of seasonal temperatures and precipitation are reconstructed using the Modern Analogue Technique with the latest version of the Eurasian Modern Pollen Database (EMPD2), which comprises numerous samples from cold environments and provides potential analogues for the LGM. The results highlight a coherent regional pattern of vegetation dynamics that appears tightly linked to winter temperature and precipitation influenced by the westerlies. Most importantly, we reconstruct high winter and annual precipitation during the LGM at all study sites, with values comparable to, or even exceeding, those estimated for the Bølling/Allerød. Our results indicate high variability in rainfall, particularly along the Atlantic margin, and lower variability further east, notably in the Alboran Sea, suggesting a climatic front located between the two regions. Two phases of increased precipitation are evidenced in our records, one from 24 to 22.5 ka and the other from 21.5 to 19.5 ka. The timing of these humid intervals is in phase with two main glacier advances in the European Alps, suggesting a consistent regional atmospheric pattern. Increased precipitation is attributed to the southward displacement of the jet stream and the westerlies due to the maximum extension of the Northern Hemisphere ice sheets. Conversely, the dry phases might correspond to a weakening or latitudinal shift of the westerlies. Indications of tenuous arboreal vegetation growth during the LGM are observed at the Iberian sites, but not at Monticchio and Xinias, where a cold climate may have prevented forest development. We hypothesize that the classic Mediterranean gradient with increasing dryness and temperature from west to east may have been amplified by the influence of the Fennoscandian and Alpine ice sheets due to the Rossby wave breaking of the jet stream west of the Alps.

1. Introduction

During Marine Isotope Stage 2 (MIS 2) (~29 – 14 ka; Lisiecki and Raymo, 2005) and the beginning of MIS 1 (until 11.7 ka), the Earth climate underwent major changes that were particularly pronounced in the North Atlantic Region, notably the Southwestern European continent (e.g., González-Sampériz et al., 2006; Fletcher and Sánchez-Goñi, 2008; Combourieu-Nebout et al., 2009; Pascual et al., 2020; Argenio et al., 2021; Rodrigo-Gámiz et al., 2022). The cold episodes defined as Heinrich Stadials (HS) HS1 and HS2 (Sanchez-Goñi and Harrison, 2010; Fletcher et al., 2010), the Last Glacial Maximum (LGM), and the last phase of the deglaciation that includes the Bølling/Allerød

---

* Corresponding author. GEOTOP, Université du Québec à Montréal, 201 av. Président-Kennedy, 7e étage, Montréal, Qc, H2X 3Y7, Canada.
E-mail address: zumaquej@gmail.com (J. Zumaque).

https://doi.org/10.1016/j.quascirev.2026.109906
Received 29 July 2025; Received in revised form 30 January 2026; Accepted 24 February 2026

(B/A) and the Younger Dryas (YD), have received special attention from paleoclimatologists and paleoceanographers (e.g., Zaragosi et al., 2001, 2006; Fletcher and Sánchez-Goñi, 2008; Combourieu-Nebout et al., 2009; Penaud et al., 2011; Toucanne et al., 2015; Pascual et al., 2020; Argenio et al., 2021) because they illustrate abrupt, large amplitude climate and ocean variations, allowing to document the dynamics of the climate-ocean system.

The LGM (23 - 19 ka; Mix et al., 2001; MARGO Project Members, 2009) is defined as the most recent time of maximum global ice volume (Mix et al., 2001), when boundary conditions were drastically different from today, with the development of large ice-sheets in the Northern Hemisphere (e.g., Dyke et al., 2002; Svendsen et al., 2004; Lambeck et al., 2006; Tarasov et al., 2012), low global sea-level of at least −120 m (Lambeck et al., 2014) and low concentration of greenhouse gas (375 ppb of CH_4, 190 ppm of CO_2) (e.g., Kageyama et al., 2017).

Paleoecological data indicate that during the LGM, cold and dry climates prevailed over most of Europe, likely due to a southward displacement of the polar front and the westerlies (e.g., Eynaud et al., 2009; Laîné et al., 2009; Toucanne et al., 2015; Beghin et al., 2016), which resulted in open vegetation such as steppe and grasslands (e.g., Peyron et al., 1998; Elenga et al., 2000; Shao et al., 2018). However, discrepancies have been highlighted for the southwestern European region, and more specifically the Iberian Peninsula, where wet conditions, especially in winter, were estimated based on proxy data (e.g., Vegas et al., 2010; Moreno et al., 2012; Schafer et al., 2016) and some model simulations (e.g., Laîné et al., 2009; Löfverström et al., 2014; Beghin et al., 2016; Löfverström and Lora, 2017; D'Agostino and Lionello, 2020; Kageyama et al., 2021) although many pollen sequences from the Pyrenean region indicated steppe vegetation and thus arid conditions (e.g., Andrieu et al., 1993; Reille and Andrieu, 1995; Valero-Garcés et al., 2004; Gonzalez-Sampériz et al., 2006). To explain such discrepancies, some authors have attributed the impact to low CO_2 atmospheric concentrations on plant water-use efficiency (Ramstein et al., 2007) and the seasonality of precipitation, as plants primarily depend on the amounts of rainfall during the growing season (Prentice et al., 1992a).

Here, we address the issue of seasonality in temperatures and precipitation over southwestern Europe from 28 to 10 ka using pollen data from three records of southern Iberia. Two of them were collected offshore, in the Atlantic (cores SU81-18; Turon et al., 2003), and the Alboran Sea (ODP Site 976; Combourieu-Nebout et al., 2009) and one is from an inland location (Padul; Camuera et al., 2018; 2019, 2021). Previous studies on the marine core SU81-18 (Turon et al., 2003) and ODP Site 976 (Combourieu-Nebout et al., 2009) have shown increased fluxes of Ericaceae pollen during the Last Glacial Maximum (LGM), which were tentatively interpreted as the result of humid conditions and relatively high temperatures compared to the surrounding HS1 and HS2 (Combourieu-Nebout et al., 2009). We revisit the pollen data from these sites and those of Padul by doing quantitative reconstructions based on the most recent Eurasian Modern Pollen Database (EMPD2; Davis et al., 2020). The EMPD2 database comprises more than 8000 samples, including many additional samples from cold environments, notably in Siberia, thus offering potential analogues for LGM conditions (Magyari et al., 2014a). Herein, we also reconstruct paleoclimate from the pollen sequences of Lago Grande di Monticchio (Allen et al., 2000; Wulf et al., 2004; Brauer et al., 2007) and Xinias (Bottema, 1979), located further east at the same latitudes, in the Central and Eastern Mediterranean basins, respectively (Fig. 1). Hence, the pollen dataset we examined comprises five lower mid-latitude sequences, allowing us to assess the regional coherency in the climatic pattern during MIS 2 and the beginning of MIS 1, and more specifically, during the LGM.

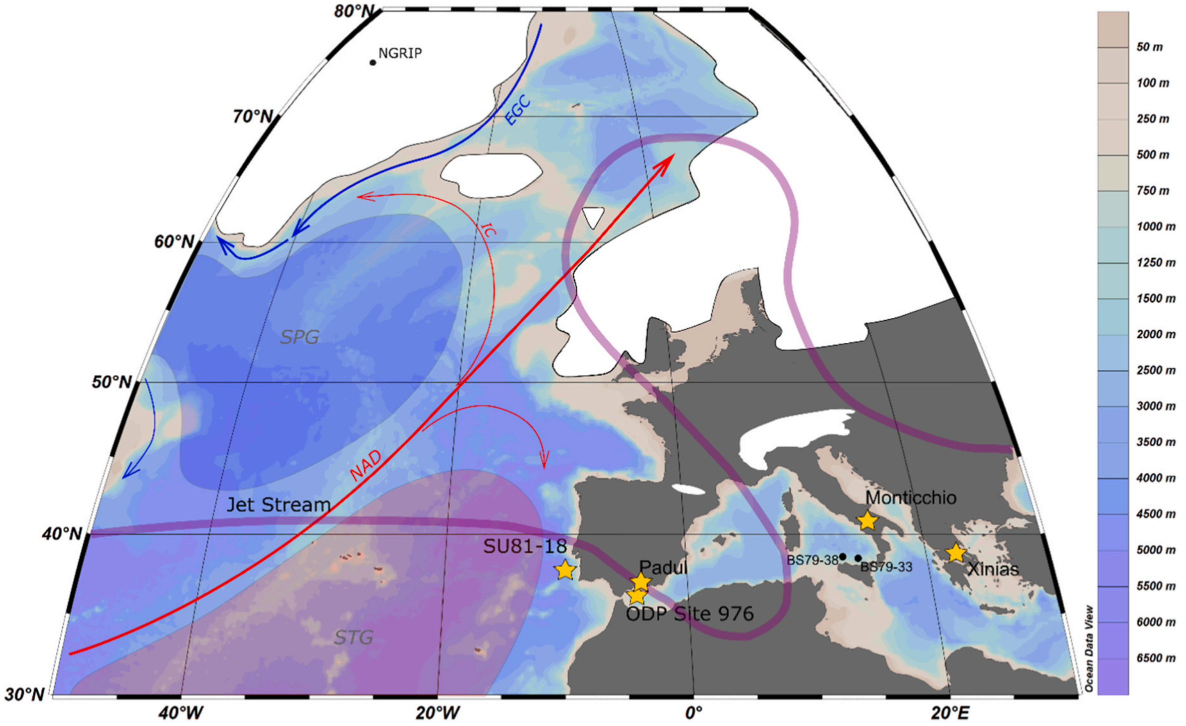

Fig. 1. Map showing the location of the five pollen sequences (yellow stars) used in this study (Table 1 and references therein). Black dots indicate the locations of records mentioned in the text: NGRIP (North Greenland Ice Core Project members, 2004), BS79-38 and BS79-33 (Cacho et al., 2001). The main surface currents and gyres are indicated as follows: Irminger Current (IC), North Atlantic Drift (NAD), East Greenland Current (EGC), Subpolar Gyre (SPG), Subtropical Gyre (STG). White areas represent LGM ice sheets. The transparent purple line defines the jet stream and notably the Rossby wave breaking west of the Alps during the LGM, as proposed and illustrated in Luetscher et al. (2015), and the schematic ice limits at LGM are defined after Ehlers and Gibbard (2004). (For interpretation of the references to color in this figure legend, the reader is referred to the Web version of this article.)

2. Environmental setting

2.1. Climate and vegetation

The five studied pollen records, located in Southwestern and Southern Europe (Fig. 1; Table 1), belong to the Mediterranean region (MedR) (~36-40°N). In winter, the regional climate is primarily influenced by the North Atlantic Oscillation (NAO), a circulation pattern characterized by the atmospheric pressure difference between the Icelandic Low and the Azores High from November to April (Hurrell, 1995). The NAO modes of variability impact the strength and direction of the westerlies. A NAO positive mode, resulting from strong pressure gradients, causes colder and drier winters in Southern Europe due to a northward displacement of the westerlies that bring moisture-laden air masses to the northwest part of the continent. Conversely, a negative mode of the NAO (i.e., weak pressure gradients) results in a milder and wetter winter climate in Southern Europe and the southward displacement of storm tracks. In the summer, the influence of the westerlies weakens, allowing anti-cyclonic cells to form over the subtropical eastern Atlantic Ocean, which generates the characteristic dry summers of the Mediterranean climate (Rodwell and Hoskins, 2001).

The above-mentioned climatic conditions favour the development of Mediterranean landscapes characterized by altitudinal gradients, which correspond to the ecological affinities of plants (Combourieu-Nebout et al., 2009, and references therein). The lowlands are characterized by evergreen sclerophyllous woodland (evergreen *Quercus*, *Olea, Pistacia, Phillyrea, Cistus*) along with steppe and semi-desert taxa (*Artemisia*, Amaranthaceae, *Ephedra*). The middle altitude vegetation mainly comprises sclerophyllous and humid-temperate oak forests (notably deciduous *Quercus* and Ericaceae), while cold-temperate coniferous forests characterize the high altitudes.

2.2. Oceanography and sedimentary processes at marine core locations

The site of deep-sea core SU81-18 (Fig. 1; Table 1) is located between 100 and 200 km off the southwestern Iberian margin, where the equatorward southern branch of the North Atlantic Drift flows (e.g., Ríos et al., 1992). A well-developed hydrographic system accounts for pollen inputs from the Tagus River area through canyons and offshore filaments (Naughton et al., 2007). There is limited airborne pollen input due to the direction of the dominant North Atlantic westerlies, but we cannot rule out the possibility of pollen dispersal from northern Africa with Saharan winds (Rodrıguez et al., 2001).

Site ODP 976 (Fig. 1; Table 1) is situated off the Southeastern Iberian Margin, in the Alboran Sea (1108 m deep), connected to the North Atlantic Ocean via the Strait of Gibraltar. The Atlantic water has lower salinity and density than the Mediterranean outflowing water, and thus occupy the upper part of the water column entering the sea from the west (La Violette, 1986, Schroeder et al., 2016). At present, there is no major river inputs in this region, but heavy rains from Southeastern Iberia may generate riverine advections to the Alboran Sea (especially via the Almeria canyon during past lowstands, e.g. Canals et al., 2004). Although the North African coast is farther away, a fluvial contribution from the North African margin cannot be ruled out during the past. Aeolian lithogenic particles only represent 12% of the total particle supply (Fabres et al., 2002). It thus implies that the main pollen contribution to this site comes essentially from the adjacent Iberian riverine system, and to a lesser degree, from the Morrocan riverine system. (Sánchez-Goñi et al., 2002). Nevertheless, the occurrence of *Cedrus* pollen from the Atlas Mountains at site ODP 976 indicates that pollen can be advected through southerly Saharan winds from northern Africa (Magri and Parra, 2002).

3. Material and methods

3.1. Pollen data and chronologies

The raw pollen data from core SU18-81, ODP Site 976, Lago Grande di Monticchio (hereafter referred to as Monticchio), and Xinias were downloaded from the ACER (Abrupt Climate Changes and Environmental Responses) database (Sánchez-Goñi et al., 2017) (Fig. 1; Table 1). The raw pollen data from the Padul sequence were shared by Camuera et al. (2018, 2019, 2021) (Fig. 1; Table 1). These sequences cover the entire MIS 2 and the beginning of MIS 1, extending to 10 ka, and offer a mean temporal resolution ranging from 95.3 to 492.9 years for the studied period (Table 1).

The advantage of studying pollen from marine cores is the usually well-constrained chronology and the possibility of direct land-sea correlations by comparing pollen and proxy indicators of the ocean environment (Sánchez-Goñi et al., 2002, 2008, 2009; Roucoux et al., 2005). Furthermore, once a sufficiently high temporal resolution is achieved, the marine time series can be correlated with the reference Greenland interstadials (GI) and stadials (GS) succession (Austin and Hibbert, 2012). For core SU81-81 and ODP Site 976, we used the same dating points as in the ACER database (for more details, see file “dating_info_ACER” in Sánchez-Goñi et al., 2017) but we recalculated the ages using CLAM (Blaauw, 2010), implemented in R (R version 3.3.1) (R Development Core Team, 2016) for consistency in the age-model of the marine and continental records (Table 1). Following Sánchez-Goñi et al. (2017), we used Marine13 (Reimer et al., 2013) to calibrate the marine sediment dates. A ΔR of 41 ± 70 yrs and −22 ± 35 yrs was used for cores SU81-81 and for ODP Site 976, respectively (for more details, see file “dating_info_ACER” in Sánchez-Goñi et al., 2017).

For the Xinias sequence, we used the updated chronology proposed in the ACER database (for more details, see Sánchez-Goñi et al., 2017). However, since the chronology of this sequence is very weak (only 5 radiocarbon dates for the period between 47 and 10 ka), the timing of the environmental changes inferred from this sequence needs to be interpreted with caution.

The age models of the three above-mentioned sequences are presented in Supplementary data (see also file “dating_info_ACER” in Sánchez-Goñi et al. (2017)).

Table 1
Marine and terrestrial pollen records used in this study.

Site name	Site type	Latitude (°N)	Longitude (°E)	Elevation (m)	Mean temporal resolution for the studied period (30 - 10 ka) (yr/sample)	References
SU81-18	Marine	37.77	−10.18	−3135	370.5	Lézine and Denèfle (1997); Turon et al. (2003)
ODP Site 976	Marine	36.2	−4.3	−1108	192.3	Combourieu-Nebout et al. (2002, 2009)
Padul	Terrestrial (wetland)	37.01	−3,6	726	124.5	Camuera et al. (2018, 2019, 2021, 2022)
Lago Grande di Monticchio	Terrestrial (lacustrine)	40.94	15.61	656	95.3	Watts et al. (1996a, 2000); Allen et al. (2000); Wulf et al. (2004); Brauer et al. (2007); Allen and Huntley (2018)
Lake Xinias	Terrestrial (lacustrine)	39.05	22.27	500	492.9	Bottema (1979)

For the Monticchio sequence, we used the initial chronology based on annual lamination ("varves") counts and sedimentological features in the non-varved intervals (Zolitschka and Negendank, 1996) as was done by the ACER group (Sánchez-Goñi et al., 2017). However, although the chronology of the entire Monticchio sequence, which covers at least the last 100,000 years, was overall corroborated by many dated tephra layers with a mean deviation of ~5% (Wulf et al., 2004), some sections appear problematic. The varve counting chronology of the lower half of the MIS 2 section may have underestimated the ages by up to 3000 years compared to the calibrated ages of the tephra layers (Wulf et al., 2004). Genty et al. (2010) have also highlighted possible offsets in the chronology of the Monticchio sequence based on speleothem data. Hence, we remain cautious regarding the interpretation of the timing of vegetation and climatic shifts at this site.

For the Padul sequence, we used the original chronology developed by Camuera et al. (2018), as presented in the associated paper.

This compilation includes 2 marine and 2 lacustrine sequences and 1 sequence retrieved from a peat bog. Consequently, all the sequences do not integrate the same spatial extent of vegetation cover. Naughton et al. (2007) have demonstrated that marine pollen samples from the western Iberian margin are very similar to adjacent estuarine pollen samples which collect pollen from the vegetation of the related hydrographic basins. Core SU81-18 mainly captures the vegetation of the hydrographic basins of the Tagus River, which represents an area of ~80,000 km^2 from Albarracin in the east to Lisbon in the west, and thus the integrated picture of the regional climate under which the vegetation has developed (Naughton et al., 2007; Sánchez Goñi et al., 2018). In the absence of large river systems, ODP Site 976 integrates vegetation signals from the Alboran Sea borderlands, specifically Spain and Morocco (Combourieu-Nebout et al., 2002, 2009), including both the coastal lowlands and the adjacent mountain ranges (Sierra Nevada and the Rif). This notably explains the pollen assemblages characterized by a mixture of arboreal taxa and open-vegetation elements. Conversely, terrestrial sequences from lakes and peat bogs primarily integrate local influxes from the catchment of the lakes or peat bogs.

3.2. *Vegetation: Plant Functional Types (PFTs)*

Since the pollen data is derived from different projects and investigators, taxonomy can vary from one site to another. Grouping the taxa reduces the number of variables and facilitates the comparison between sites. We thus converted the pollen taxa into Plant Functional Types (PFTs), which are broad classes of plants defined by stature, leaf form, phenology and climatic thresholds, following the concept developed by Prentice et al. (1992). The three fossil records were consequently harmonized in 94 taxa to characterize 15 arboreal and 8 shrub/herbaceous plant functional types (PFTs) (Table 2), with each taxon assigned to only one PFT based on the known biology of the species (Peyron et al., 1998). Virtual PFTs, which represent a combination of the potential PFTs that a taxon could belong to, were initially created to handle ambiguous taxa and were subsequently reassigned depending on the biome identified from the pollen sample (Peyron et al., 1998). In this study, for each pollen sample, the relative abundances of the 94 pollen taxa were calculated (Table 2) and then square-root transformed to emphasize the importance of rare versus more abundant taxa. We summed the square-rooted relative abundances of the taxa associated with their respective PFTs (Table 2) and calculated percentages from the scores obtained for each PFT. Unlike Prentice et al. (1996) and Peyron et al. (1998), we did not exclude taxa with low abundances (<0.5%).

3.3. *Pollen-based climate reconstruction*

We reconstructed climate parameters from pollen data using the Modern Analogue Technique (MAT) (Overpeck et al., 1985; Guiot, 1990). MAT is based on the principle that the ecological affinities of the different species have not changed through time (Jackson and Overpeck, 2000) and compares a fossil pollen assemblage to all modern pollen assemblages in a reference database. The similarity assessment between fossil and modern pollen assemblages is based on the squared chord distance (SCD) dissimilarity metric (Overpeck et al., 1985), which ranges from 0 to 2. Low values indicate a high degree of similarity, while high values indicate a significant degree of dissimilarity between two samples. The 5 closest modern pollen samples defined by the lowest SCDs, are the best analogues. The average of their climate parameter values is calculated after weighting inversely to the SCDs to provide information on past climatic conditions. An SCD threshold beyond which any analogue is rejected is also calculated based on the Monte Carlo method. In this work, we followed de Vernal et al. (2005) for a reliability index of analogues which defines three categories: 1) Poor or no analogue situation when the SCD of the closest analogue is higher than the SCD threshold, 2) Acceptable analogue situation when the SCD is between half of the threshold value and the threshold, and 3) Good analogue situation when the SCD is between 0 and half of the threshold value.

Table 2

Assignments used for the PFTs. Codes in green represent arboreal PFTs while those in brown represent non-arboreal PFTs.

Codes	PFTs	Taxa included in PFTs
EC	Eurythermic conifer	*Pinus, Pinus* subgen. *Diploxylon*
ECPI	Eurythermic conifer/ Pioneer	*Juniperus*
BS	Boreal summergreen	*Larix*
PI	Pioneer	*Betula*
BEC	Boreal evergreen conifer	*Picea, Pinus* subgen. *Haploxylon*
BCTC	Boreal evergreen/cool-temperate conifer	*Abies*
CTC1	Intermediate temperate conifer	*Cedrus, Taxus*
TSAA	Temperate/boreal summergreen/arctic-alpine	*Alnus, Salix*
TSBS	Temperate/boreal summergreen	*Populus*
TS	Temperate summergreen	*Acer, Fraxinus, Fraxinus excelsior, Quercus* (deciduous)
TS1	Cool-temperate summergreen	*Carpinus, Corylus, Fagus, Frangula, Tilia, Ulmus*
TS2	Warm-temperate summergreen	*Castanea, Fraxinus ornus, Juglans, Ostrya, Platanus,* Rhamnaceae, *Vitis*
WTE	Warm-temperate broad-leaved evergreen	*Quercus* (evergreen)
WTE1	Cool-temperate broad-leaved evergreen	*Buxus, Hedera, Ilex*
WTE2	Warm-temperate sclerophyll trees/shrub	*Acacia, Arbutus, Cistus, Mercuria,* Myrtaceae, *Olea, Phillyrea, Pistacia, Rhus*
AA	Arctic-alpine dwarf shrub	*Alnus fructicosa, Betula nana, Dryas, Empetrum, Rhododendron, Saxifraga, Vaccinium*
COGS	Cold grass shrub	*Hippophaë, Polygonum*
H	Heath	*Calluna,* Ericaceae
GR	Grass	Poaceae
WAGS	Warm grass shrub	Brassicaceae, *Ceratonia,* Crassulaceae, *Echium, Ephedra fragilis,* Fabaceae, *Galium,* Scrophulariaceae, *Zizyphus*
SF	Steppe forb/shrub	Apiaceae, *Armeria, Artemisia, Carduus,* Campanulaceae, Caryophyllaceae, *Centaurea,* Cyperaceae, Dipsacaceae, *Filipendula, Helianthemum, Plantago,* Plumbaginaceae, *Ranunculus,* Rosaceae, *Rosmarinus,* Rubiaceae, *Rumex, Sanguisorba, Thalictrum,* Urticaceae, *Viburnum*
SFDF	Steppe/desert forb/shrub	Boraginaceae, Compositae, Compositae *tubuliflore,* Compositae *liguliflore,* Zygophyllaceae
DF	Desert forb/shrub	Amaranthaceae, *Ephedra, Ephedra distachya*

The paleoclimate reconstructions were made with the "bioindic" package (ftp://ftp.cerege.fr/R/Package_bioindic/), built on the Rplatform (http://cran.r-project.org/), using a modern calibration dataset taken from version 2 of the Eurasian Modern Pollen Database (EMPD2; Davis et al., 2020). This subset of data includes 7634 modern pollen samples from the Paleartic realm and a total of 88 pollen taxa. It covers a total of nine biomes (cf. Davis et al., 2020). It thus comprises a large number of potential modern analogues for different climates and vegetation types, which is particularly critical when considering the objective of climatic reconstructions of glacial times (Magyari et al., 2014a; Davis et al., 2022). The climatic data in the initial EMPD2 were calculated using WordlClim2 (Fick and Hijmans, 2017) and include mean monthly, seasonal and annual temperatures and precipitation (Davis et al., 2020) averaged over the interval 1970 - 2000 (Fick and Hijmans, 2017). We added the mean temperature of the warmest (MTWA) and the coldest months (MTCO), and the seasonality defined as the difference between MTWA and MTCO. MTWA, MTCO, seasonality, along with winter (Pdjf), summer (Pjja) and annual precipitation (Pann) were the climatic variables retained for this work. This ready-to-use version of the EMPD2 is presented in Zumaque et al. (2025a) and available on Pangaea (Zumaque et al., 2025b; https://doi.org/10.1594/PANGAEA.973997). We are aware that not all of the selected climatic parameters have the same ecological relevance for plant growth. During summer, the precipitation–evaporation balance plays a key role, as plant evapotranspiration capacity becomes critical, whereas water availability during the growing season, i.e. in spring, is equally crucial for plant growth (Prentice et al., 1992a). Although reconstructions of spring and autumn precipitation will not be presented here, these parameters will be briefly addressed in the discussion.

Due to the overrepresentation of *Pinus* in marine sediments (Turon, 1984; Rochon and de Vernal, 1994), the modern calibration dataset was adapted for the data treatment of the two marine series of this study. We removed *Pinus* and recalculated the relative abundances of taxa (%). Since we had already removed samples with a sum (excluding *Pinus*) $<$ 100 grains, the “marine version” of our adapted dataset comprises the same number of modern samples as the “terrestrial” version of the dataset. The rationale for applying the Modern Analogue Technique (MAT) to marine pollen sequences and excluding *Pinus* from modern and fossil assemblages is detailed in Zumaque et al. (2025c).

Validation tests were conducted to estimate the accuracy of quantitative reconstructions using the two final versions of our sub-dataset (with and without *Pinus*, i.e., with 87 or 88 taxa), and the results are presented in Table 3. We have used a set of 5 analogues, which seems to be the most appropriate number for quantitative reconstructions (mainly for statistical relevance and robustness reasons), as shown by validation tests performed by Zumaque et al. (2025c).

Atmospheric CO_2 concentration influences vegetation dynamics by controlling plant water-use efficiency (Harrison and Prentice, 2003; Prentice et al., 2017). Therefore, atmospheric CO_2 variations likely impacted the relationships between pollen assemblages and climate, especially during glacial times when atmospheric CO_2 concentration values were low (Ahn and Brook, 2008; Bauska et al., 2021). Many have argued that it was essential to account for CO_2 changes when reconstructing climate parameters from vegetation proxies, especially for periods with low CO_2 concentrations, such as the LGM, during which climate estimates from pollen were possibly biased toward drier values (e.g., Cleator et al., 2020; Prentice et al., 2022). The fact that MAT, as many other paleoclimate approaches, does not account for the atmospheric CO_2 effect is thus a limitation. In a recent study, Davis et al. (2022) compared MAT reconstructions with reconstructions from a method that accounts for CO_2 changes (i.e., Inverse Modelling; Guiot et al., 2000) during the Last Glacial Maximum (LGM) in Europe and other regions. The results show good agreement between the two methods, strengthening the reliability of MAT for climatic reconstructions of glacial times and suggesting that low CO_2 concentrations during the LGM had little impact on pollen-based climate reconstructions (Davis et al., 2022).

Table 3
Accuracy of MAT reconstructions estimated from the root mean square error of prediction (RMSEP) and the coefficient of correlation (R^2) for the 88 and 87 (*Pinus* excluded) taxa databases. MTCO: mean-temperature of the coldest month in °C; MTWA: mean-temperature of the warmest month in °C; Pdjf: winter precipitation in mm; Pjja: summer precipitation in mm; Pann: annual precipitation in mm; Seasonality: MTWA – MTCO in °C.

Climatic parameters	RMSEP		R^2	
	88 taxa	87 taxa (without *Pinus*)	88 taxa	87 taxa (without *Pinus*)
MTCO	3.41	3.52	0.91	0.91
MTWA	1.95	1.94	0.83	0.83
Seasonality	3.44	3.51	0.88	0.87
Pdjf	68.76	71.65	0.76	0.74
Pjja	46.34	47.34	0.79	0.79
Pann	199.79	204.84	0.76	0.75

MAT reconstructions are compared to modern values at the terrestrial sites using the mean climatic values calculated from 1901 to 2022 with Climate Explorer (https://climexp.knmi.nl/start.cgi). The grid for the climatic compilation is 0.5° × 0.5°. Because pollen in marine sediment cores may correspond to fluxes from wide areas, it is difficult to assess the modern climatic values at the two study marine sites.

3.4. Redundancy analysis (RDA)

A redundancy analysis (RDA) was performed for each site, incorporating PFT and paleoclimatic estimates, using Canoco 5 software (Šmilauer and Lepš, 2014). It allows us to 1) examine the primary variation patterns of the vegetation (PFTs) and 2) to better visualize which climatic parameters explain the primary variation patterns in the vegetation. Because square-root transformations were applied to the initial pollen percentages for the PFT grouping, no further transformation was made before running the RDAs. The goal here is not to demonstrate that vegetation responds to climate, as this is a fundamental principle of climate reconstruction based on paleobotanical data, but rather to investigate the nature of the climate-vegetation linkages in the study region during Marine Isotope Stage 2 (MIS 2). It is also worth highlighting here that the paleoclimatic reconstructions are based on pollen taxa instead of grouped taxa, as is the case for the PFTs, and that the number of taxa retained for PFT grouping and MAT is different.

3.5. Paleohydrographic reconstructions at sites SU81-18 and ODP976

Planktonic foraminifera assemblages were previously analyzed for the SU81-18 core (Turon et al., 2003) and the ODP Site 976 (Eynaud, F., unpublished). The results were already used to infer paleohydrographic conditions in previous studies (e.g, Penaud et al., 2011; Eynaud et al., 2013), but for this article, new paleohydrographic reconstructions were calculated based on the latest version of the foraminifera modern database and using the MAT1007 transfer function developed at EPOC after the MARGO (Multiproxy Approach for the Reconstruction of the Glacial Ocean Surface) exercise conducted in the 2000s (see Eynaud et al., 2018, 2021 for a review on this approach). The set of reconstructed parameters has been recently enlarged thanks to an update of modern hydrographic references (see the methods in de Vernal et al., 2020; Eynaud et al., 2021), providing diverse reconstructions for monthly, seasonal, and annual sea-surface parameters.

Here, we selected summer and winter sea-surface temperature (SST) reconstructions at zero meters (tsum0m and twin0m, respectively) and mean annual sea-ice cover (SIC, as the mean annual sea-ice concentration expressed as a percentage of coverage, ranging from 0 to 100%). They were obtained with a root mean squared error of prediction (RMSEP) of 1.3 °C for SST and of 10% for annual SIC.

Calculations derived from past assemblages rely on the Modern Analogue Technique (MAT) applied to a modern reference database of 1007 sediment surfacesamples in the North Atlantic Ocean and its adjacent seas. Relative abundances (%) calculated for each species were used to reconstruct hydrographical parameters using the script developed by Guiot & Brewer for the R software (i.e., derived from the bioindic package for MAT calculations, https://www.eccorev.fr/spip.php?article389). A statistical assessment of the distance (or dissimilarity) between the fossil and modern assemblages led to the identification of the five best modern analogues and the estimation of hydrographical parameters from an average weighted inversely to the distance of analogues (exactly as it was done for pollen derived reconstructions).

4. Results

The redundancy analysis (RDA) graphs for all sites are presented in Fig. 2, while Figs. 3–7 present the RDA-Axis 1 scores over time alongside the paleoclimatic reconstructions for cores SU81-18, ODP Site 976, Padul, Monticchio and Xinias, respectively.

4.1. Primary patterns of PFT variations

The redundancy analysis (RDA) applied to the PFT and climatic reconstructions informs us on the primary patterns of PFT variation at each site (Fig. 2). The RDA-Axis 1 explains 60.57, 73.5, 84,80 and

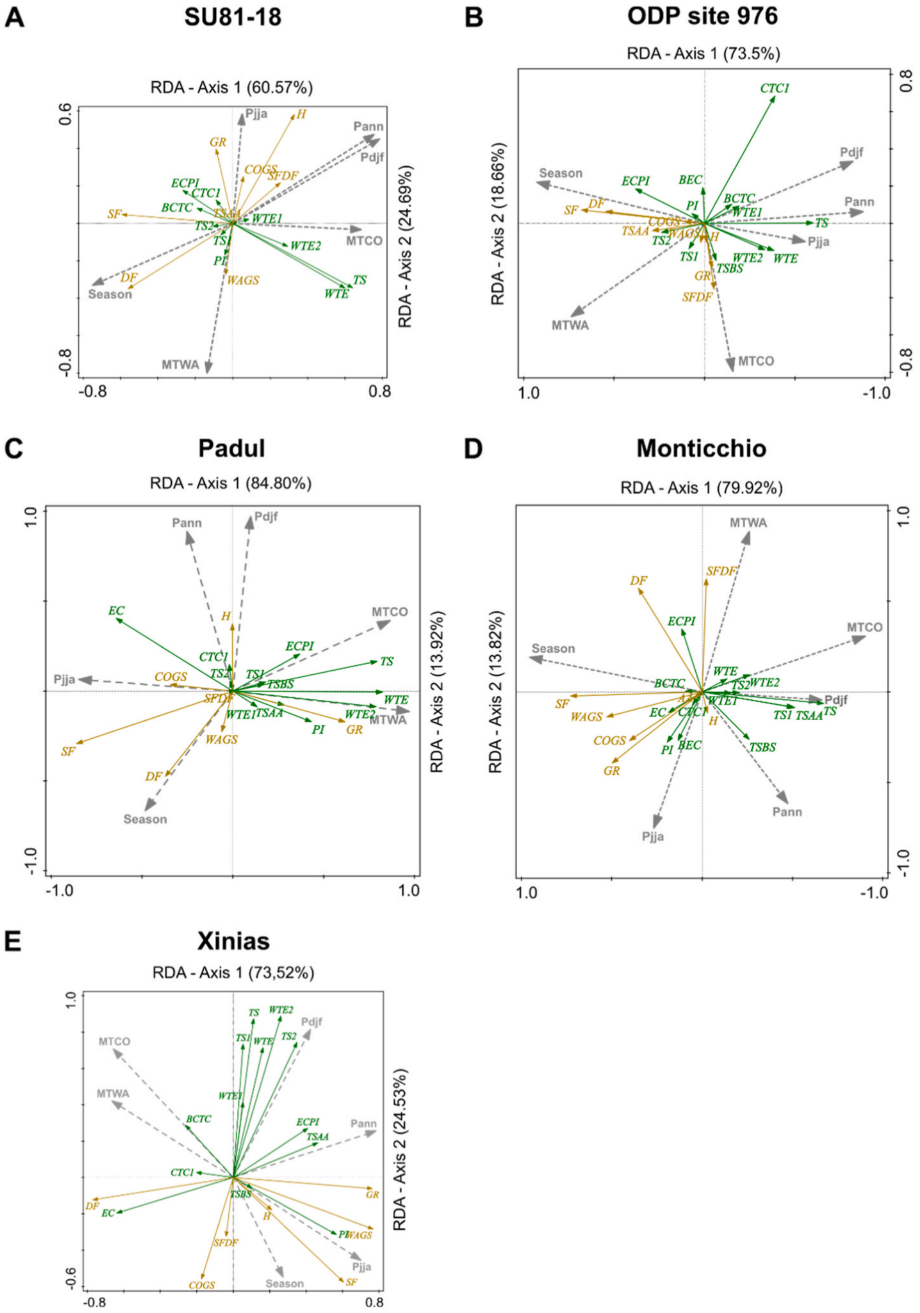

Fig. 2. Results of the redundancy analysis (RDA) in the 4 study sequences. a) SU81-18 off South Portugal (Turon et al., 2003); b) ODP Site 976 in Alboran Sea (Combourieu-Nebout et al., 2009); c) Padul in Southeastern Spain (Camuera et al., 2018, 2019); d) Monticchio in Southern Italy (Allen et al., 2000) and e) Xinias in Greece (Bottema, 1979). Green and yellow arrows represent the arboreal and non-arboreal PFTs, respectively (Table 2). Grey dashed arrows represent the climatic parameter discussed in this paper. Climatic parameters as in Table 3. (For interpretation of the references to color in this figure legend, the reader is referred to the Web version of this article.)

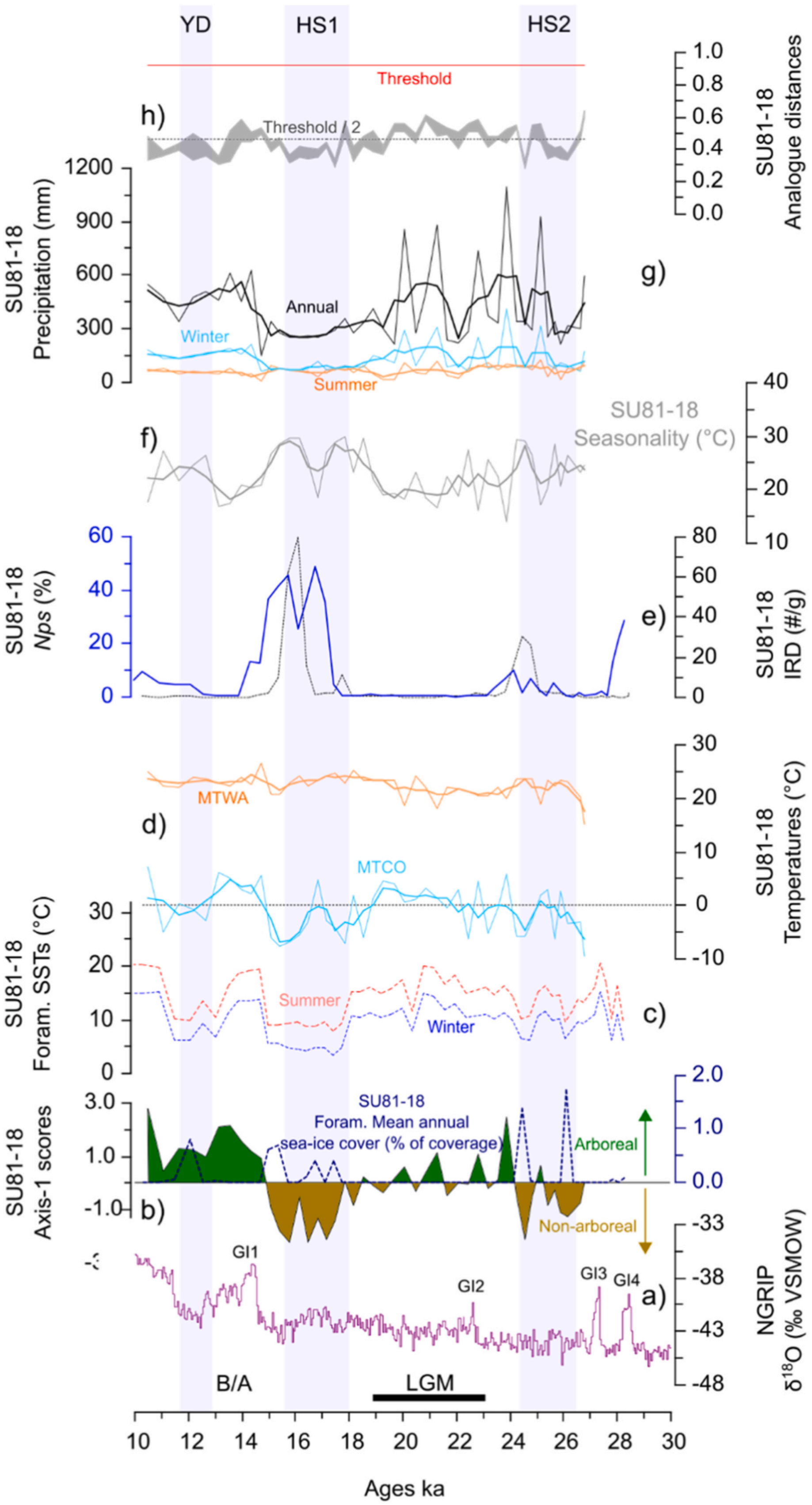

(caption on next page)

Fig. 3. Records related to vegetation, sea-surface conditions, and pollen-based climate reconstructions at site SU81-18 (Fig. 1; Table 1). a) NGRIP reference oxygen isotope record (North Greenland Ice Core Project members, 2004), b) RDA axis-1 scores (see Fig. 2a) and foraminifera-based mean annual sea-ice cover (see Material and Methods), c) foraminifera – based Sea-Surface Temperatures (SSTs) (this study, see Section 3.5.), d) Mean temperature of the coldest (MTCO) and the warmest months (MTWA), e) *Neogloboquadina pachyderma* (Nps) percentages in planktic foraminifer assemblages (Eynaud et al., 2009) and IRD (Bard et al., 2000), f) Seasonality (MTWA-MTCO), g) annual and seasonal precipitation, h) square-chord distances of the 1st and 5th best analogues and analogue thresholds (see text). Light curves: MAT values; Bold curves: 3-point running mean. The blue zones correspond to the Heinrich Stadials (HS) as defined in Sánchez-Goñi and Harrison (2010) and the Younger Dryas (YD) as defined in Rasmussen et al. (2014). (For interpretation of the references to color in this figure legend, the reader is referred to the Web version of this article.)

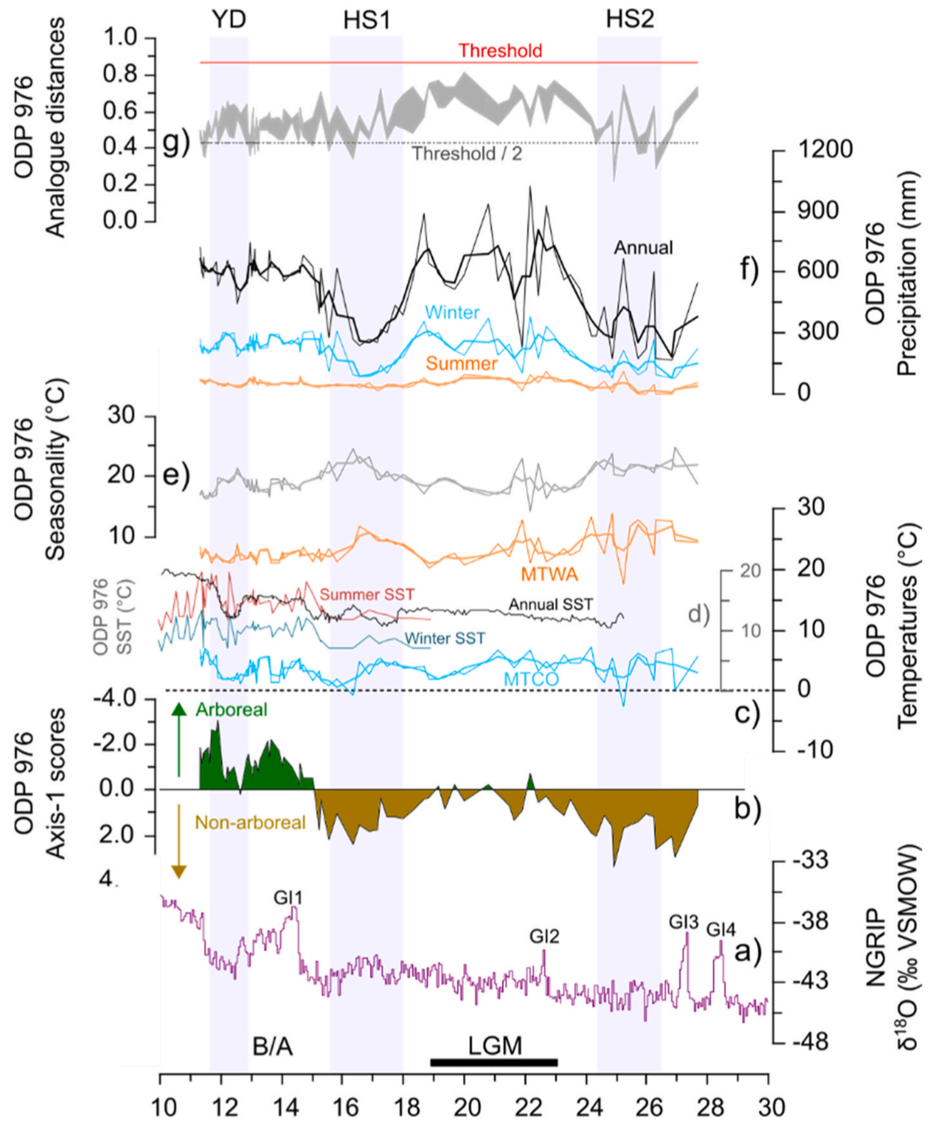

Fig. 4. Records related to vegetation, sea-surface conditions, and pollen-based climatic reconstructions at ODP Site 976 (Fig. 1; Table 1). a) reference NGRIP oxygen isotope record (North Greenland Ice Core Project members, 2004), b) RDA axis-1 scores (see Fig. 2b), c) Mean temperature of the coldest (MTCO) and the warmest months (MTWA), d) planktonic foraminifera-based Sea-Surface Temperatures (SSTs) (summer and winter; this study) and alkenone-based mean annual SSTs (Martrat et al., 2014), e) Seasonality (MTWA-MTCO), f) annual and seasonal precipitation and g) square-chord distances of the 1st and 5th best analogues and analogue threshold values (see text). Light curves: MAT values; Bold curves: 3-point running mean. The blue zones correspond to the Heinrich Stadials (HS) as defined in Sánchez-Goñi and Harrison (2010) and the Younger Dryas (YD) as defined in Rasmussen et al. (2014). (For interpretation of the references to color in this figure legend, the reader is referred to the Web version of this article.)

79.92% of the total PFT variance of data in core SU81-18, at ODP Site 976, Padul and Monticchio, respectively. Hence, we consider axis 1 as reflecting the primary pattern of vegetation variation.

Axis 1 indicates an opposition between arboreal and non-arboreal PFTs (Fig. 2). At the marine locations of core SU81-18 and ODP Site 976 (Fig. 2a and b), Temperate summergreen (TS), Warm Temperate Broad-Leaved Evergreen (WTE) and to a lesser degree Warm-temperate sclerophyll trees/shrub (WTE2) constitute the arboreal PFTs displaying the most substantial variability. They are opposed to Steppe forb/shrub (SF), Desert forb/shrub (DF) and, to a lesser extent, *Juniperus* (ECPI; Table 2). The same PFTs are opposed at Padul, with the addition of the Eurythermic conifer (EC), i.e., *Pinus*, which was removed from the marine sequences (see Material and Methods). These PFTs are comparable to the non-arboreal PFTs in the Padul RDA graph (Fig. 2c). At Monticchio, the arboreal PFTs TS, Cool-Temperate summergreen (TS1) and Temperate/boreal summergreen/arctic-alpine (TSAA) are opposed to

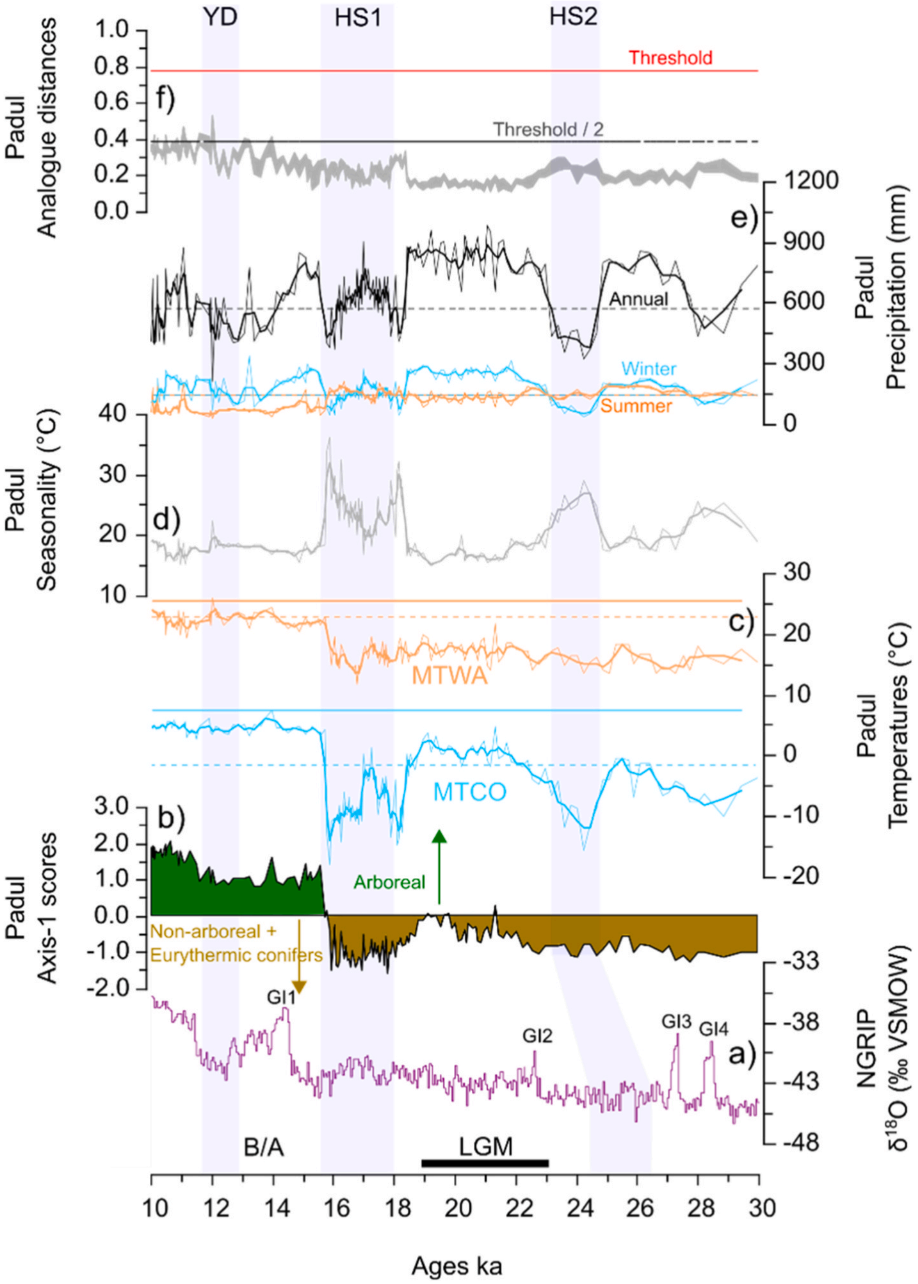

Fig. 5. Records related to vegetation and pollen-based climatic reconstructions at Padul (Fig. 1; Table 1). a) reference NGRIP oxygen isotope record (North Greenland Ice Core Project members, 2004), b) RDA axis-1 scores (see Fig. 2c), c) Mean temperature of the coldest (MTCO) and the warmest months (MTWA), d) Seasonality (MTWA-MTCO), e) annual and seasonal precipitation and f) square-chord distances of the 1st and 5th best analogues and analogue threshold values (see text). Dashed color horizontal lines in c and e represent the mean 1901-2022 climate values obtained with Climate Explorer (https://climexp.knmi.nl/start.cgi) from a 0.5° × 0.5° grid (see Material and Methods), while continuous color horizontal lines in c represent the mean January and July temperatures measured for the 2001-2022 and 2001-2021 periods respectively at the Padul weather station (see Section 4.2.2). The blue zones indicate the Heinrich Stadials (HS) and the Younger Dryas (YD). For all records, the YD is defined following Rasmussen et al. (2014), while the HS are reported on the NGRIP record as defined by Sánchez-Goñi and Harrison (2010). Apparent offsets in the timing of HS in other records likely reflect chronological uncertainties. (For interpretation of the references to color in this figure legend, the reader is referred to the Web version of this article.)

SF, Cold (COGS) and Warm grass shrubs (WAGS) and Grass (GR) (Fig. 2c).

At Xinias, RDA-Axis 1 also represents the primary pattern of vegetation variation, accounting for 73.52% of the total variance (Fig. 2e). However, at this site, the opposition between arboreal and non-arboreal PFTs is reflected along Axis 2, which records 24.53% of the total variance. We will thus use also the second RDA axis for comparison with other sites in the discussion.

4.2. *Vegetation and climate during the glacial episode*

The primary (and secondary for Xinias) patterns of PFT variations through time (Axis-1 scores) and the results of MAT reconstructions for SU81-18, ODP Site 976, Padul, Monticchio and Xinias are presented in Figs. 3–7 respectively, together with ocean proxy data from the same sites in the case of marine sequences and from adjacent sites in case of Monticchio.

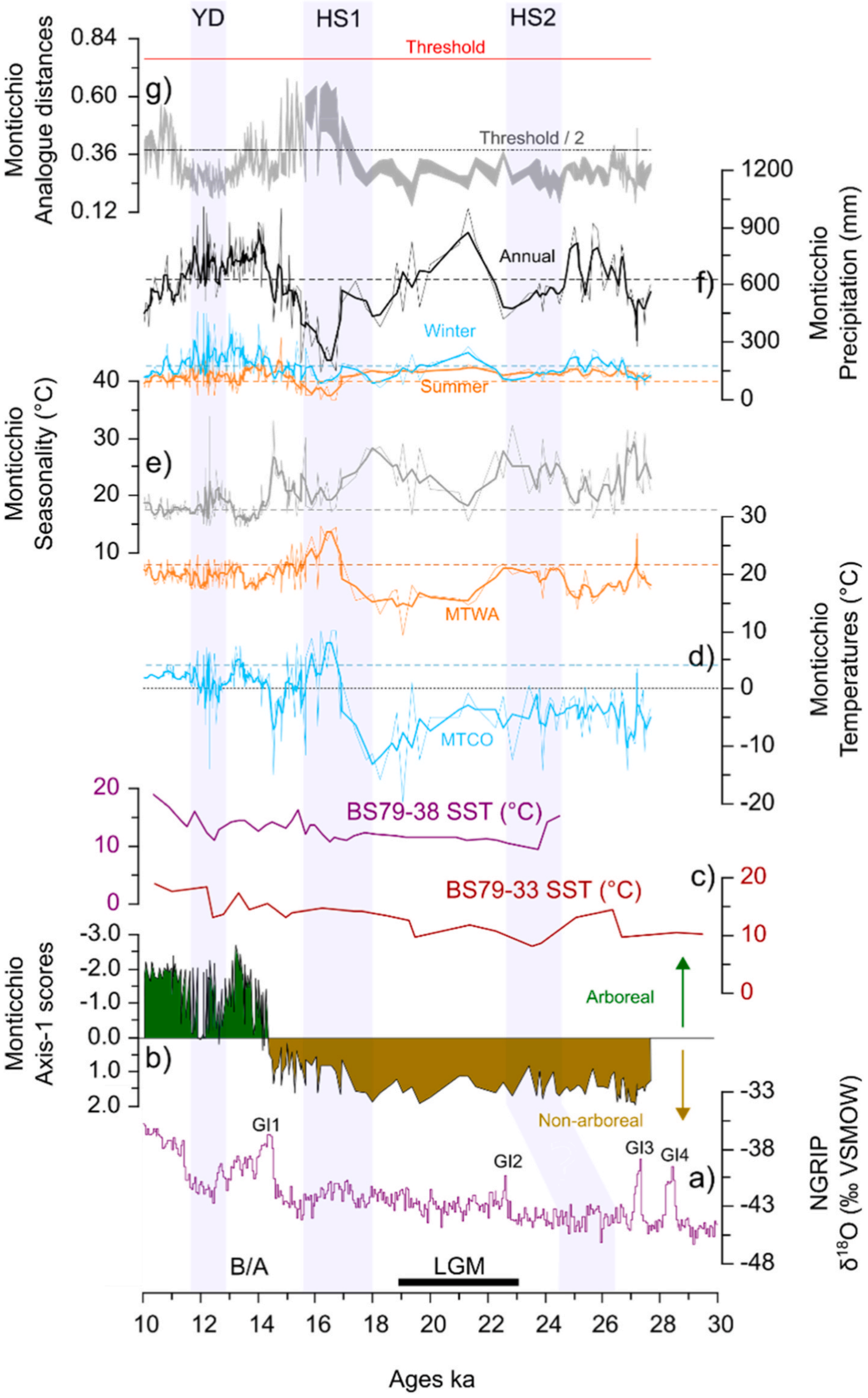

Fig. 6. Records related to vegetation, and pollen-based climatic reconstructions at Monticchio (Fig. 1; Table 1) and sea-surface conditions from proximal marine cores. a) reference NGRIP oxygen isotope record (North Greenland Ice Core Project members, 2004), b) RDA axis-1 scores (see Fig. 2d), c) Alkenone-based mean annual Sea-Surface Temperatures (SSTs) from cores BS79-33 and BS79-38 located in Tyrrhenian Sea (Cacho et al., 2001), d) Mean temperature of the coldest (MTCO) and the warmest months (MTWA) (MAT), e) Seasonality (MTWA-MTCO) (MAT), f) annual and seasonal precipitation (MAT) and g) square-chord distances of the 1st and 5th best analogues and threshold values for significant analogue (see text). Light curves: MAT values; Bold curves: 3-point running mean. Dashed color lines in d, e and f represent the mean 1901-2022 climate values (see Material and Methods). The blue zones indicate the Heinrich Stadials (HS) and the Younger Dryas (YD). For all records, the YD is defined following Rasmussen et al. (2014), while the HS are reported on the NGRIP record as defined by Sánchez-Goñi and Harrison (2010). Apparent offsets in the timing of HS in other records likely reflect chronological uncertainties. (For interpretation of the references to color in this figure legend, the reader is referred to the Web version of this article.)

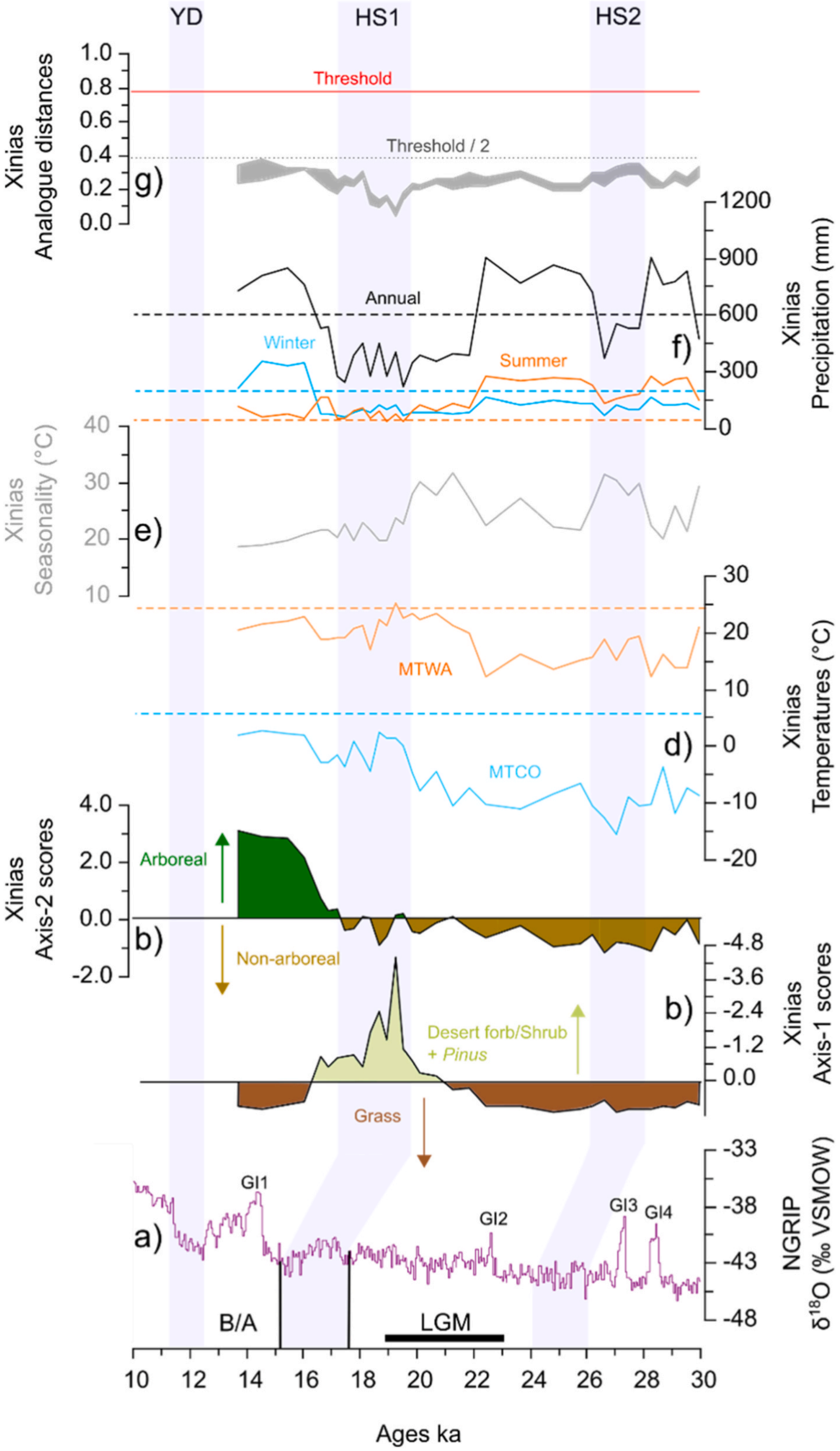

Fig. 7. Records related to vegetation and pollen-based climatic reconstructions at Xinias (Fig. 1; Table 1). a) reference NGRIP oxygen isotope record (North Greenland Ice Core Project members, 2004), b) RDA axis-1 scores (see Fig. 2e), c) RDA axis-2 scores (see Fig. 2e), d) Mean temperature of the coldest (MTCO) and the warmest months (MTWA), e) Seasonality (MTWA-MTCO), f) annual and seasonal precipitation and g) square-chord distances of the 1st and 5th best analogues and analogue threshold values (see text). Dashed colour lines in c and e represent the mean 1901-2022 climate values (see Material and Methods). The blue zones indicate the Heinrich Stadials (HS) and the Younger Dryas (YD). For all records, the YD is defined following Rasmussen et al. (2014), while the HS are reported on the NGRIP record as defined by Sánchez-Goñi and Harrison (2010). Apparent offsets in the timing of HS in other records likely reflect chronological uncertainties. (For interpretation of the references to color in this figure legend, the reader is referred to the Web version of this article.)

4.2.1. Southwestern Iberian margin

The primary pattern of vegetation variations in core SU81-18 depicts significant variations (Fig. 3b), with the lowest proportions of arboreal vegetation being recorded during HS2 and HS1, while the highest proportions of arboreal PFTs characterize the upper section (~15 to 10 ka) (Fig. 3a and b). Between HS2 and HS1, which encompasses the LGM, high amplitude variations are recorded around moderately high proportions of arboreal vegetation.

Arboreal PFTs are positively linked with MTCO (Figs. 2a and 3d) and, to a lesser degree, with Pann and Pdjf, both being highly correlated (Figs. 2a and 3g). However, there is no apparent relationship between the PFTs and Pjja (Figs. 2a and 3g) and MTWA (Figs. 2a and 3d). Hence, the MAT reconstructions suggest a predominant influence of the winter season on the vegetation.

MTCO exhibits significant variability, with an amplitude of approximately 10 °C and several incursions below 0 °C (Fig. 3d), which may have constituted ecological stress on the vegetation, favouring the decline of arboreal vegetation. An IRD peak, which corresponds to the Heinrich layer (Sánchez-Goñi and Harrison, 2010), accompanies the low MTCO in the latest phase of each HS (Fig. 3e; Bard et al., 2000). Positive MTCO characterizes the B/A, the middle part of each HS and the intervals between HS, which encompasses the LGM, despite a few incursions below 0 °C around 22.5 and 19 ka (Fig. 3d). Overall, the 3-point running mean of MTCO is in good agreement with foraminifera-based SST curves (Fig. 3c), demonstrating close linkages between land and ocean conditions. The only noticeable exception is the MTCO peak recorded around 17 ka during HS1, which has no correspondence in the SST record nor the relatively high percentages (50%) of *Neogloboquadrina pachyderma* (Fig. 3e; Eynaud et al., 2009), indicating almost polar conditions at this time. The close land-ocean linkage is further shown by the discrete peaks of sea-ice occurrence inferred from planktonic foraminifer assemblages mirroring the most significant development of steppe vegetation that occurred during the HSs.

Throughout the entire section, pollen-based estimates of summer temperatures remain similar, and seasonality mirrors the MTCO (Fig. 3d and f), with higher values during the cold HSs and YD, while lower seasonality characterizes the LGM (Fig. 3f).

Annual and winter precipitation appear highly correlated (Figs. 2a and 3g), with Pann mimicking Pdjf, albeit with a three times greater amplitude. The lowest values of Pann and Pdjf (around 300 and 100 mm, respectively) are recorded during HS1 and the first half and the very end of HS2 (Fig. 3g). In contrast, moderately higher values characterize the MIS 1 section, with only a slight decrease during the cold YD. The most noticeable feature of the Pann and Pdjf records is, however, the significant millennial-scale variability that characterizes the period from 25.5 to 19.5 ka, and thus the LGM, with 5 peaks reaching the highest values of the entire sequence (Fig. 3g). Most of these peaks are concomitant with the MTCO peaks recorded during this same period (Fig. 3d).

4.2.2. Alboran Sea and Southeastern Spain

The primary patterns of PFT variations at ODP Site 976 (Fig. 4b) and Padul (Fig. 5b) show two highly distinguishable sections: the first one, until ~15 ka, is characterized by high proportions of non-arboreal vegetation. The other, after 15 ka, is marked by increased arboreal vegetation. The HS2 records the highest proportions of non-arboreal PFTs. It is followed by a progressive decrease of the non-arboreal vegetation during the LGM until 19 ka, after which the proportions of treeless PFTs increase again, with high values during HS1 (Fig. 4a and b and 5a-b). After 15 ka, afforestation characterizes the B/A at both sites. However, the decrease of the arboreal PFTs recorded at ODP Site 976 during the following YD is less acute at Padul. The beginning of the Holocene, at ~11.7 ka, is then marked by the highest rates of arboreal vegetation in both sequences (Fig. 4a and b and 5a-b).

In the Alboran Sea, the RDA graph (Fig. 2b) shows a strong linkage between arboreal PFTs and precipitation indicators (Pann, Pjja, and Pdjf), which are highly correlated. Non-arboreal PFTs appear strongly correlated with seasonality, but also, although to a lesser extent, with MTWA. Conversely, MTCO does not seem to significantly influence the primary pattern of PFT variation, as it is strongly correlated with Axis 2 (Fig. 2b). Conversely, at Padul, in Southeastern Spain, arboreal PFTs appear more correlated with both winter and summer temperatures, while winter and annual precipitation are strongly correlated with Axis 2 (Fig. 2c).

Pann and Pdjf show strong correlations and similar behaviour at both southeastern Iberian sites ODP Site 976 and Padul (Figs. 4f and 5e). Overall, Pann and Pdjf record their lowest values during the HSs, although Padul records an increase of Pann and Pdjf during the middle part of HS1 and the highest values during the LGM. The drop in annual precipitation recorded in the Padul sequence between 24.7 and 23 ka, which we attribute to HS2, could indicate an underestimation of the ages for the bottom section (Fig. 5). It is worth mentioning that the period between HS2 and HS1, which encompasses the LGM, was characterized by high-amplitude variations in precipitation at ODP Site 976, with low values around 22 ka (Fig. 4f). In contrast, more stable conditions were recorded at Padul. The period after 15 ka recorded relatively high and stable values at ODP Site 976, except for a slight decrease during the first part of the YD Fig. 4f) which corresponds to a peak in *Artemisia* and other steppe elements, while the second part of the YD is marked by an increase in *Cedrus* which induces a change in precipitation (Combourieu-Nebout et al., 2009). In contrast, Pann at Padul mimics the NGRIP record, with more pronounced decreased values during the YD (Fig. 5a and e).

The primary difference between the two sequences is evident in temperature estimates. This may be because the ODP Site 976 pollen record integrates a regional signal, whereas Padul probably records a more local signal or a superimposition of local and regional signals. ODP Site 976 shows minor temperature variations, with an amplitude rarely exceeding 6 or 7 °C for both MTCO and MTWA (Fig. 4c). MTCO remains mostly positive throughout the sequence with only slight decreases during the second halves of HS2 and HS1, at the end of the LGM, and during the YD. SST estimates (Fig. 4d) depict variations of similar amplitude (~5 °C). SSTs inferred from planktonic foraminifera (this study; Fig. 4d), and especially winter SSTs, display trends very similar to MTCO from 19 to 10 ka, with notably higher values during the first part of HS1 and B/A, supporting our pollen-based temperature reconstructions. Alkenone-based mean annual SSTs (Fig. 4d; Martrat et al., 2014) also exhibit a similar behaviour for the upper part of the study section (~18 to 10 ka), but with lower values during the first part of HS1 compared to the second part. It is worth noticing that, overall, these mean annual SST values equal the summer SSTs inferred from foraminifera, although the latter do not cover the lower part of the sequence (Fig. 4d). They, however, depict a general trend of an increase of almost 10 °C from the LGM to the Holocene, which is not apparent in our pollen-based temperature estimates or in the foraminifera-based SST records. The MTCO at Padul exhibits large temperature drops (between 10 and 15 °C) during HS1 and HS2, while temperatures above 0 °C characterize the LGM and the beginning of MIS 1. In Fig. 5c, the MTCO values appear higher than those of modern samples (~0 °C). However, modern values have been inferred from a 0.5° × 0.5° grid, and Padul is located at the foothills of the Sierra Nevada, which culminates at 3479 m asl (Camuera et al., 2018, 2019, 2021). They may thus be underestimated, as confirmed by climatic data from the Padul weather station (https://www.juntadeandalucia.es/agriculturaypesca/ifapa/riaweb/web/estacion/18/10), which indicates an average January temperature (MTCO) of 7.6 °C for the period 2002-2022 and an average July temperature (MTWA) of 25.4 °C for the period 2001-2021. The MTWA remains relatively warm and stable until 15 ka, 5 °C below the inferred modern values, which is in better agreement with the aforementioned values reported by the Padul weather station, although still slightly underestimated (Fig. 5c). At 15 ka, an increase of approximately 5 °C brings the MTWA close to modern values.

4.2.3. Southern Italy

The PFT results at Monticchio (Fig. 6b) highlight high proportions of non-arboreal PFTs during MIS 2, before afforestation. However, no afforestation is visible between the HSs (Fig. 6a and b), and a slight increase in arboreal PFTs is depicted from about 17 ka to 14.5 ka, after which the rapid shift toward dominant arboreal PFTs marked the beginning of the B/A. A slight decrease in arboreal PFTs around 12 ka likely corresponds to the opening of the forest canopy, as indicated by the regional signature of the YD (Fig. 6a and b).

The redundancy analysis results at Monticchio (Fig. 2d) indicate a high correlation between arboreal PFTs and winter precipitation (Pdjf) and MTCO, while non-arboreal PFTs depict strong linkages with seasonality. As in core SU81-18, Pjja and MTWA do not appear to be related to this primary pattern of PFTs, as both are strongly correlated with Axis 2.

Pollen-based estimates show variable but negative MTCO until about 17 ka (Fig. 6d). Relatively steady conditions from approximately 28 to 21 ka, and a general decrease of MTCO toward minimum values are estimated afterwards until 18 ka. The MTWA remained unchanged, thus reflecting increased seasonal temperature gradients. In the interval at the beginning of HS1, there is a trend from very negative to positive MTCO values, approaching modern values, which is surprisingly high given the stadial context. It should be viewed with caution due to the chronological uncertainties (Wulf et al., 2004; Genty et al., 2010) and also because the analogues exhibit high SCDs (Fig. 6g). The selected modern analogues of this interval may correspond to warm steppes, characterized by low precipitation but high temperatures (Tarasov et al., 2012). It is worth noting that the modern values calculated in this study are similar to those presented in Watts et al. (1996b). Positive MTCO was recorded during the arboreal vegetation phases (Fig. 6b and d), which likely correspond to the B/A and Holocene, whereas slightly lower values (around 0 °C) were recorded during the YD.

The MTWA signal exhibits variations that are generally parallel to those of MTCO, but with lower amplitude, resulting in significant changes in seasonality that globally mirror the MTCO curve (Fig. 6d). As for MTCO, the MTWA values are close to the modern ones at the beginning of MIS 1 (Fig. 6d).

According to the chronological frame used herein, high Pann and Pdjf characterize the HS2, the interval from 22 to 18.5 ka and MIS 1 (Fig. 6f). In contrast, the lowest values are recorded during the second half of HS1 and after HS2. These odd estimates might result from an underestimation of the ages, particularly in the first half of the MIS 2 section, where a shift of about 2000 - 3000 years, as evidenced by Wulf et al. (2004), would permit a better correspondence of dry conditions with HS2, and would suggest that the preceding Pann and Pdjf peaks belong to GI 3 and GI 4.

The mean annual SSTs recorded in two marine sediment cores located near the Tyrrhenian Sea (Fig. 1; Cacho et al., 2001) exhibit variations that are distinct from pollen-based temperature reconstructions. The SSTs from both cores BS79-38 and BS79-33 (Figs. 1 and 6c; Cacho et al., 2001) show low amplitude variations but display a general warming trend, like the mean annual SST inferred at ODP Site 976 (Fig. 4d; Martrat et al., 2014). They do not exhibit significant cooling pulses during HS1 and HS2, and there is a low-amplitude SST decrease corresponding to the YD. The comparison of the marine record and Monticchio data could illustrate a decoupling between ocean conditions and inland climate.

4.2.4. Greece

MIS 2 at Xinias was characterized by high proportions of non-arboreal PFTs, with no apparent growth of forest vegetation between HSs but a slightly increasing trend of arboreal vegetation from 28 to 17 ka (Fig. 7a and b). After 17 ka, the pollen data indicate afforestation, the precise age of which is difficult to assess due to poor dating control of the upper part of the sequence (see Material and Methods and Fig. S3 in Supplementary data).

Increased arboreal vegetation was related to increased winter precipitation and, to a lesser extent, temperatures, while non-arboreal PFTs correspond to high seasonality (Fig. 2e).

Annual precipitation (Pann) exhibits significant variations throughout the sequence, with high values (between 800 and 900 mm) from 30 to 28 ka, 26 to 22 ka, and from 17 to the top of the section, and low values in between (Fig. 7e). The low values (~350–550 mm) observed between 28 and 26 ka could likely correspond to HS2 and indicate an overestimation of the ages in the bottom half of the Xinias sequence as well (Fig. 7). The second period of low Pann seems to be divided into 2 phases. However, the low temporal resolution may bias this interpretation: a first phase from 22 to 20 ka with relatively stable values around 400 mm and a second phase from 20 to 17 ka, with values ranging from 250 to 450 mm. Given that the second phase records the lowest values and directly precedes the significant afforestation attributed to the B/A, we suggest that it corresponds to HS1 (Fig. 7). It is worth noting that, conversely to MIS 1, during MIS 2, summer precipitation appears higher than winter precipitation. This must be regarded with caution, considering that, at present, precipitation in the region is almost exclusively restricted to all seasons but summer (Bottema, 1979).

Overall, pollen-based temperature estimates show increasing values throughout the sequence, with negative MTCO values from 30 to 20 ka.

5. Discussion

5.1. Regionally coherent winter-annual precipitation pattern from 28 to 10 ka

The present-day vegetation in Southern Europe is highly dependent on winter precipitation (Gouveia et al., 2008), which is closely linked to the North Atlantic Oscillation (NAO), a circulation pattern characterized by the atmospheric pressure difference between the Icelandic Low and the Azores High (Hurrell, 1995). The NAO index is calculated for the coldest months of the year, from November to April, when its variability is at its highest (Hurrell, 1995; Hurrell et al., 2003). A negative mode of the NAO, characterized by weak pressure gradients, induces a southward displacement of the westerlies, resulting in mild and wet winters in southwestern Europe. Conversely, a positive phase of the NAO, characterized by strong pressure gradients, causes a northward displacement of the westerlies, bringing moist air masses to northwest Europe and leading to cold and dry winters in southern Europe. In summary, the NAO is related to latitudinal displacements of the North Atlantic Jet Stream (Hurrell, 1995; Hurrell et al., 2003).

Vegetation changes at most sites (Fig. 2) exhibit a strong dependence on winter and annual precipitation, which positively correlate. High winter and annual precipitation favour afforestation, while dry conditions lead to the opening of the forest cover. Conversely, summer precipitation appears to be weakly correlated with winter and annual precipitation (Fig. 2). The decoupling between winter and summer precipitation may be related to differences in rainfall types. Many LGM studies have demonstrated that winter precipitation is associated with westerly storms, whereas summer precipitation has a more local convective origin (Laîné et al., 2009; Beghin et al., 2016; Del Gobbo et al., 2022). Camuera et al. (2022), who investigated pollen-based seasonal precipitation over the last 200,000 years at Padul (Fig. 1), also demonstrated an anticorrelation between summer and winter-annual precipitation. Here, we propose that part of the autumn and spring precipitation reflects processes governing winter precipitation and relates to the westerlies, thereby explaining why annual precipitation exhibits the same behaviour as winter precipitation but with a tripled amplitude (Fig. 8). This could also explain the apparent relationship between the forest development and winter and annual precipitation, since plant growth primarily depends on rainfall and water availability during the growing season, which is centered in spring (e.g., Prentice, 1992a). The absence of a clear dependence or anticorrelation between arboreal vegetation and summer climatic parameters in the

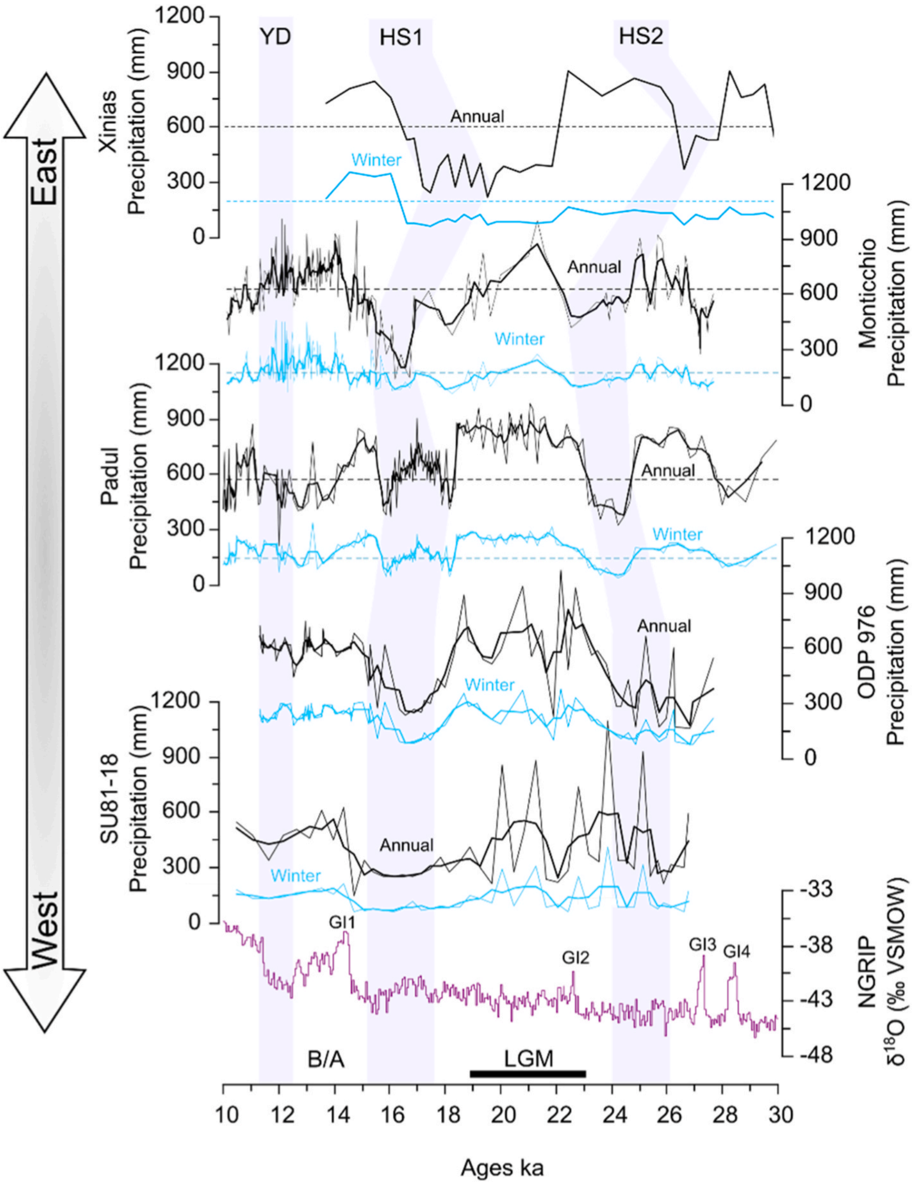

Fig. 8. Pollen-based winter (Pdjf) and annual precipitation (Pann) estimates from the 5 studied sequences. Light curves: MAT values; Bold curves: 3-point running mean, except for Xinias where it represents MAT values. Dashed blue and black lines represent the mean 1901-2022 climate values for winter and annual precipitation, respectively (see Material and Methods). The blue zones indicate the Heinrich Stadials (HS) and the Younger Dryas (YD). For all records, the YD is defined following Rasmussen et al. (2014), while the HS are reported on the NGRIP record as defined by Sánchez-Goñi and Harrison (2010). Apparent offsets in the timing of HS in other records likely reflect chronological uncertainties. (For interpretation of the references to color in this figure legend, the reader is referred to the Web version of this article.)

RDA plots (Fig. 2) suggests that the summer precipitation–evaporation balance was not a limiting factor for plant growth during the LGM.

Despite chronological uncertainties and temporal lags between records, winter and annual precipitation (Fig. 8) exhibit generally coherent regional patterns. Very low rainfall is recorded during HSs, although the marine core SU81-18 and ODP Site 976 record high-amplitude peaks within HS2, and the Padul site records high values within HS1. A general increase in both Pdjf and Pann is observed from HS1 to B/A. After the B/A transition, precipitation remains almost uniform at site ODP 976, with only a slight decrease during the first half of the YD (Fig. 8), displaying a two-phase structure as previously highlighted by other authors (Combourieu-Nebout et al., 2009). Sites SU81-18 and Padul record a more pronounced decrease in precipitation during YD, mimicking the NGRIP record. In Italy, the Monticchio record is much noisier at that time, making it difficult to draw any conclusions, except for a decreasing trend at the beginning of the Holocene, which should be interpreted with caution due to the high SCDs of the analogues (Fig. 6g).

5.1.1. *Regional increase in winter-annual precipitation during the LGM*

One of the most striking features of the five studied sequences is the high values of Pdjf and Pann during the LGM (Fig. 8). The LGM interval between HSs exhibits substantial variability, with peaks of ~375 mm and 900 mm for Pdjf and Pann, respectively, in marine core SU81-18 and ODP Site 976 (Fig. 8). At ODP Site 976, these values lie well above the relatively high estimates previously inferred by Combourieu-Nebout et al. (2009) for the same sequence during the LGM period (+300 mm and +100 mm for Pann and Pdjf, respectively). However, the remainder of the Pann and Pdjf records remain broadly comparable in terms of anomaly relative to the early Holocene (Combourieu-Nebout et al., 2009). It is worth noting that these high precipitation values correspond to high SCDs in both studies (Figs. 3h and 4g of this study; Fig. 6 in

Combourieu-Nebout et al., 2009), indicating only an acceptable analogue situation for LGM reconstructions (see Material and Methods section 3.3). This may be related to the pollen assemblage, which displays a combination of *Cedrus*, Cichorioideae, and Ericaceae that is rarely represented in modern analogue datasets. Padul also records its highest precipitation values during the LGM, with annual precipitation reaching ~900 mm, well above the modern values (Fig. 8; see also Camuera et al., 2018). While high precipitation occurred before HS2 and after HS1 at Monticchio and Xinias, further east, the LGM was characterized by similarly elevated annual precipitation, especially during its initial phase (Figs. 6 and 7).

Our reconstructed winter-annual precipitation estimates are consistent on a regional scale for the LGM and appear well above modern values (+300 mm for annual precipitation), at least for the three terrestrial sites (Fig. 8). The LGM assemblages at the five sites share very few common modern analogues, although most of them come from similar ecoregions. The more distant analogues for the highest reconstructed values usually present annual precipitation values between 550 and 700 mm, close to the modern ones, implying that an overestimation of our LGM precipitation values cannot be ruled out. However, the closest analogues are associated with precipitation values above 900 mm. At Site SU81-18, the highest precipitation values are mainly inferred based on analogues from the Cantabrian mixed forests. At ODP Site 976, the high precipitation values relate to analogues from the Northwest Iberian montane forests, the Aegean and Western Turkey sclerophyllous and mixed forests, and the Cantabrian mixed forests. At the high elevation site of Padul, analogues are from the Pyrenees conifer and mixed forests, the Northwest Iberian montane forests and the Alps conifer and mixed forests, where annual precipitation of about 900 mm is presently recorded. At Monticchio, analogues are also from the Pyrenees conifer and mixed forest, as well as the Cantabrian mixed forests and the Northwest Iberian montane forest. Finally, at Xinias, the high values are mainly generated by analogues from the Eastern Anatolian montane steppe.

In contrast to our estimate here, a dry climate in Southern Europe was often inferred for the LGM. Many continental pollen sequences from the Pyrenean region indicate dry conditions and dominant steppe vegetation (e.g., Reille and Andrieu, 1995; Valero-Garcés et al., 2004; Gonzalez-Sampériz et al., 2006) (Fig. 9). García-Amorena et al. (2007) also reconstructed low annual precipitation along the Portuguese coast based on macrofossil remains. Lécuyer et al. (2021) inferred drier and colder conditions from stable isotope measurements on tooth enamel carbonate of Cervidae, Equidae and Caprinae in France and Spain (Fig. 9).

Some proxies instead suggest increased moisture in Southern Europe during the LGM compared to the surrounding HSs. For example, leaf wax data from paleosols in central Spain, near the Tagus River, indicate humid conditions associated with the presence of drought-intolerant deciduous trees (Schafer et al., 2016) (Fig. 9). Many marine sequences off the Portuguese coast (Roucoux et al., 2005; Naughton et al., 2007) and in the Alboran Sea (Fletcher and Sánchez-Goñi, 2008), including ODP Site 976 (Combourieu-Nebout et al., 2009) record the presence of Ericaceae during the LGM, which is characteristic of humid conditions. Further south, increased moisture was also inferred from high river levels in northern Morocco (El Amrani et al., 2008). High lake levels were reported in the Iberian Peninsula and attributed to reduced evapotranspiration resulting from colder temperatures associated with low summer insolation (Moreno et al., 2012; Camuera et al., 2018, 2019) (Fig. 9). Although evapotranspiration may have decreased during this period, we cannot exclude an increase in precipitation as well, especially since many proxies from the Iberian Peninsula region indicate warmer conditions during the LGM than during the surrounding HE 1 and 2 (e.g., de Abreu et al., 2003; Combourieu-Nebout et al., 2009; Vegas et al., 2010; Penaud et al., 2011). High lake levels have also been reported in Italy (Giraudi, 2017). Following the present west-east climate gradient of the Mediterranean Basin with drier conditions to the east, steppic, semi-desertic and desertic vegetation prevailed in the eastern Mediterranean Basin, although a slight increase of tree pollen compared to the surrounding HEs is visible during the LGM (Langgut et al., 2011). In the same region, colder and drier conditions than present-day ones were also deduced from speleothem data (e.g., Bar-Matthews et al., 1997, 1999) (Fig. 9). However, Bar-Matthews et al. (1999) identify a peak of δ^{18}O at 18-19 ka as the LGM, whereas the values from H2 (identified at 26 ka) to 19 ka appear lower, reflecting a slight improvement in climatic conditions. In this regard, it is important to note that in many earlier studies, due to poor chronological control, changing definition of the LGM (from CLIMAP project members (1981) to EPILOG (Mix et al., 2001)) or simple misinterpretation, Heinrich Stadial 1 has been mistaken for the LGM.

Climate model simulations similarly span a wide range of climatic responses in southern and southwestern Europe, from drier to wetter conditions compared to the pre-industrial period (e.g., Kageyama et al., 2021), and the region remains a zone of mismatch between model simulations and proxy-based reconstructions. Still, many modelling

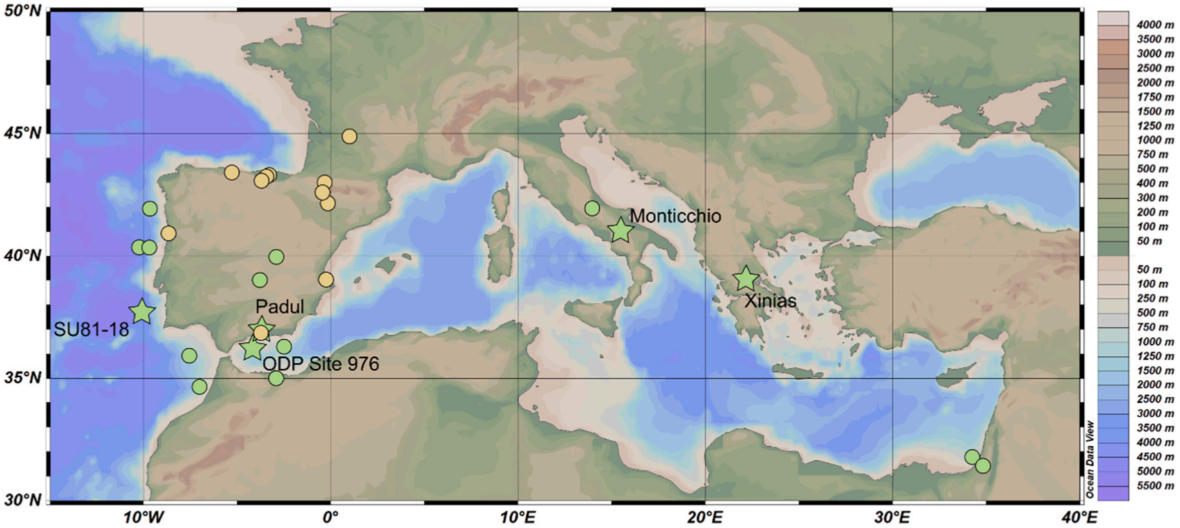

Fig. 9. Illustration of the climatic conditions inferred from the proxies mentioned in Section 5.1.1 for the LGM period (23 - 19 ka; Mix et al., 2001). Brown dots indicate cold and/or dry conditions, whereas green dots indicate relatively mild and/or wet conditions. (For interpretation of the references to color in this figure legend, the reader is referred to the Web version of this article.)

experiments suggest a wetter climate over southwestern Europe during the LGM, and particularly over the Iberian Peninsula (e.g., Laîné et al., 2009; Löfverström et al., 2014; Beghin et al., 2016; Löfverström and Lora, 2017; D'Agostino and Lionello, 2020; Kageyama et al., 2021). More importantly, they show evidence of increased winter precipitation, with some even simulating higher winter precipitation during the Last Glacial Maximum (LGM) than during the pre-industrial period (e.g., Beghin et al., 2016). Although we must remain cautious regarding a possible overestimation of our precipitation values during the LGM, and we cannot directly compare our climatic reconstructions from the marine sites with modern climate (see Section 3.3), Pdjf and Pann (Fig. 8) at both sites show higher values during the LGM than during the early Holocene. The high winter precipitation over Iberia during the LGM has mainly been attributed to the southeastward shift of the North Atlantic storm-track because of the presence of the Laurentide and Fennoscandian ice sheets (e.g., Kageyama et al., 1999; Laîné et al., 2009; Luetscher et al., 2015; D'Agostino and Lionello, 2020; Pinto and Ludwig, 2020). Enhanced precipitation from the westerlies was possibly favoured by relatively high SSTs at middle latitudes during the LGM, while the HSs were marked by cold pulses (e.g., de Abreu et al., 2003; de Vernal et al., 2005; Eynaud et al., 2009; Penaud et al., 2011). In this regard, Penaud et al. (2011) showed that the relatively high sea-surface temperature reconstructions obtained off the southwestern Iberian Peninsula from dinocysts, foraminifera, and alkenones for the LGM period were also consistent with PMIP2 model results (Kageyama et al., 2006). Further east, many studies of glacier advance in the Alps during the LGM point to a southward shift of the North Atlantic Jet stream that would have increased moisture advection, thus contributing to building up the glaciers to their maximum extent (e.g., Spötl et al., 2021; Ribolini et al., 2022; Roattino et al., 2023; Del Gobbo et al., 2022). There is, however, an ongoing debate on whether the precipitations were dominantly from the North Atlantic via the westerlies or from the Mediterranean Sea due to pronounced Rossby-wave breaking west of the Alps (Fig. 1) (e.g., Luetscher et al., 2015; Lofverstrom, 2020; Spötl et al., 2021; Ribolini et al., 2022; Del Gobbo et al., 2022). Regardless of the origin of the precipitation, our results suggest that relatively high precipitation, particularly in winter, during the LGM was a regional feature of southern Europe.

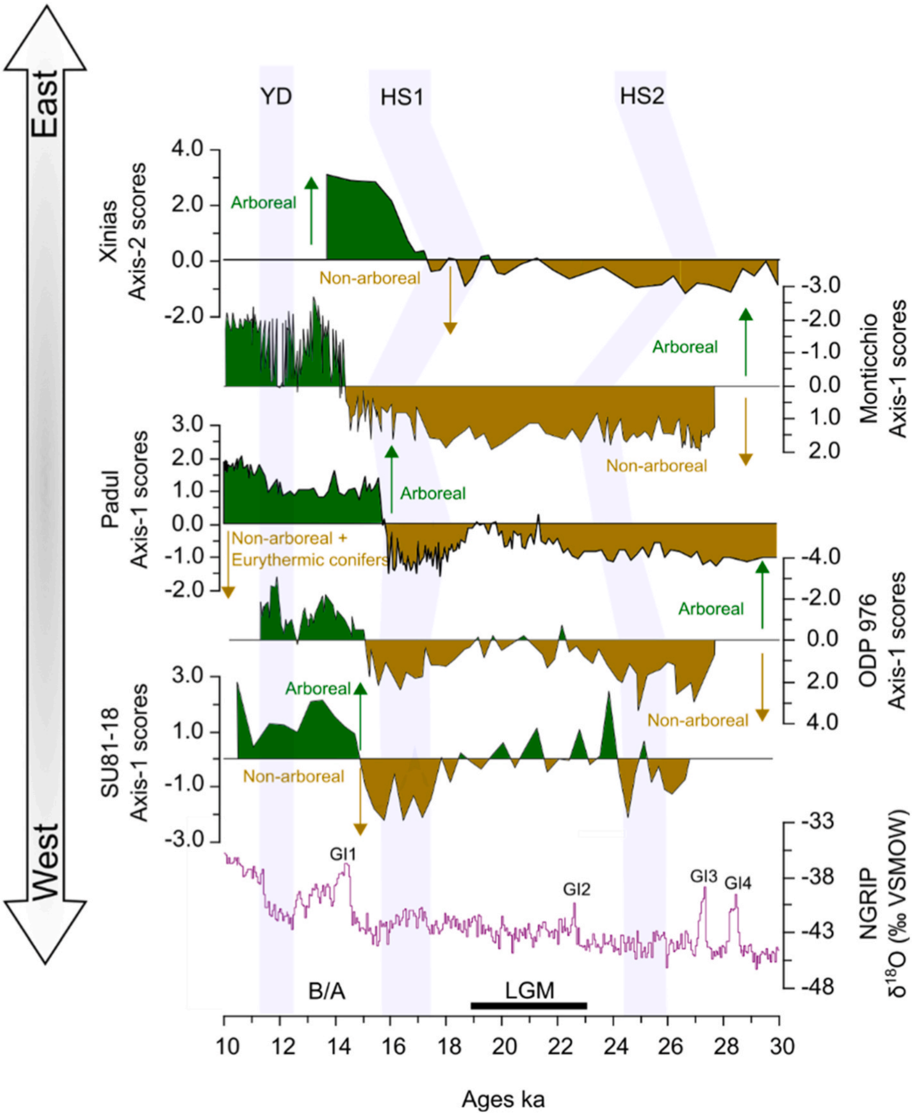

Fig. 10. NGRIP oxygen isotope record (North Greenland Ice Core Project members, 2004) and RDA axis-1 scores (axis-2 scores for Xinias, see also Fig. 2 and text) of the record from the five studied pollen sequences (Fig. 1; Table 1). The blue zones indicate the Heinrich Stadials (HS) and the Younger Dryas (YD). For all records, the YD is defined following Rasmussen et al. (2014), while the HS are reported on the NGRIP record as defined by Sánchez-Goñi and Harrison (2010). Apparent offsets in the timing of HS in other records likely reflect chronological uncertainties. (For interpretation of the references to color in this figure legend, the reader is referred to the Web version of this article.)

Another possible origin of high precipitation values is related to atmospheric rivers, i.e., narrow corridors of high moisture content and heat transport (Shields et al., 2019). Skinner et al. (2023) highlighted that during the Last Glacial Maximum (LGM), the frequency of atmospheric river precipitation was generally lower than in the preindustrial period, except at mid-latitudes (~35°N) in the North Atlantic and the Iberian Peninsula, where it appears to have been higher. Skinner et al. (2023) also suggested that these atmospheric rivers were responsible for the high precipitation over the Iberian Peninsula as inferred by many model simulations (e.g., Beghin et al., 2016). However, the results of Skinner et al. (2023) do not show higher precipitation further east in the Mediterranean basin, contrary to our pollen-based reconstructions (Fig. 8) or the model simulation results of glacier advance in the Alps (e.g., Luetscher et al., 2015; Lofverstrom, 2020; Spötl et al., 2021; Ribolini et al., 2022; Del Gobbo et al., 2022).

5.2. *Vegetation dynamics in southern Europe during the LGM and West-East gradient of winter temperatures*

The five study sequences yielded regionally consistent climate changes for the YD, B/A and HSs (Fig. 10). High values of winter-annual precipitation are reconstructed for the southern Iberia, Italy, and Greece sites during the LGM, between HSs. Still, there is an apparent west-east gradient in vegetation (Fig. 10). There is no evidence of afforestation from 28 to 17 ka at Xinias and Monticchio, in contrast to records from Padul and ODP Site 976 in Southeastern Iberia, where a slight decrease in non-arboreal vegetation is noted. Afforestation was apparently more pronounced in the Atlantic sector, with peaks in arboreal PFTs reaching values comparable to those of the B/A (Fig. 10). Despite differences in afforestation rates between the southeastern and southwestern Iberian sites, arboreal vegetation expanded across the southern Iberian Peninsula during the LGM. This aligns with the mean state of LGM vegetation as reconstructed from pollen sequences by Davis et al. (2022), which shows high proportions of moisture-sensitive deciduous taxa and xerophytic woodlands in southern Iberia.

Further east, at Monticchio and Xinias the PFTs show no evidence of afforestation from 28 to 17 ka, including the LGM (Fig. 10). This concurs with the LGM vegetation reconstructions by Davis et al. (2022), with steppe occupying central and southern Italy and the development of steppe, semi-desertic or desertic vegetation reported further east in the Mediterranean Basin (Tzedakis et al., 2004; Langgut et al., 2011; Davis et al., 2022). Still, both Monticchio and Xinias sites recorded high

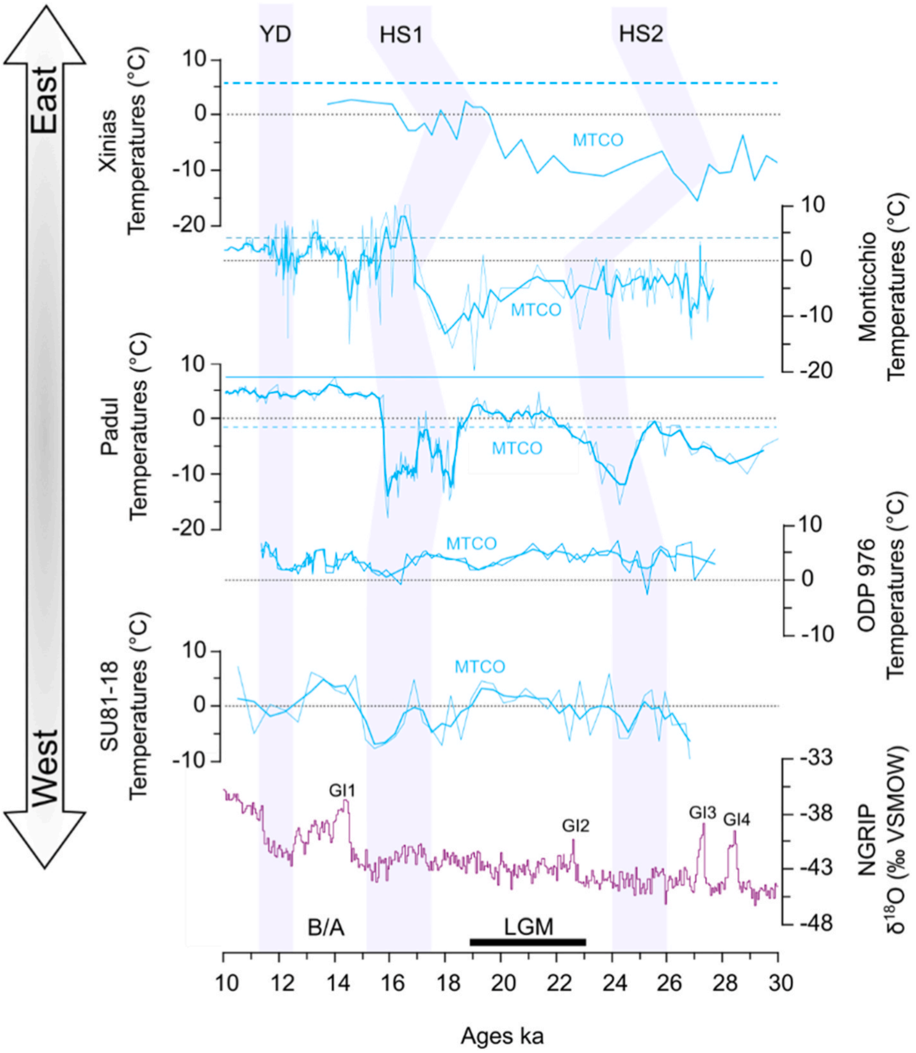

Fig. 11. Pollen-based mean temperature of the coldest month (MTCO) estimates from the 5 studied sequences. Light curves: MAT values; Bold curves: 3-point running mean. The blue zones correspond to the Heinrich Stadials (HS) as defined in Sánchez-Goñi and Harrison (2010) and the Younger Dryas (YD) as defined in Rasmussen et al. (2014). The blue zones indicate the Heinrich Stadials (HS) and the Younger Dryas (YD). For all records, the YD is defined following Rasmussen et al. (2014), while the HS are reported on the NGRIP record as defined by Sánchez-Goñi and Harrison (2010). Apparent offsets in the timing of HS in other records likely reflect chronological uncertainties. (For interpretation of the references to color in this figure legend, the reader is referred to the Web version of this article.)

annual and winter precipitation (Fig. 8), thus potentially high precipitation in spring, the primary growing season. An increase in rainfall was also detected in the East Carpathian Mountains, where the proportion of wet-tundra vegetation cover increased (Magyari et al., 2014b), thus supporting the hypothesis of a large, regionally coherent pattern regarding winter-annual precipitation. However, contrary to the Iberian sites, negative MTCO values, substantially lower than modern ones, were reconstructed for the entire section at Monticchio and Xinias (Figs. 10 and 11), which could have constituted ecological stress and hampered the growth of arboreal vegetation (Prentice, 1992a). Although at present, the Mediterranean Basin shows a clear climatic gradient with increasing dryness and temperature from west to east, low MTCO, concomitant to the coldest MTWA (Figs. 6d and 7c) further east during the LGM, were possibly amplified by the influence of the Fennoscandian and Alpine ice sheets, due to the potential Rossby wave breaking of the jet stream west of the Alps (Fig. 1; Luetscher et al., 2015). According to Löfverström and Lora (2017), the significant change in the vegetation at Monticchio and Xinias after 15 ka, concomitant with warmer MTCO, could relate to a large-scale atmospheric reorganization caused by the splitting of the Laurentide Ice Sheet and the Cordilleran Ice Sheet. Under such conditions, the Rossby wave over Central Europe would have decreased (Fig. 1; Luetscher et al., 2015), while the shrinking of the Northern Hemisphere ice sheets favoured a northward displacement of the jet stream.

5.3. *Highly variable climate conditions in southwestern Europe during the LGM*

The Atlantic Sector exhibits high variability in vegetation as shown by PFTs data during the LGM, likely in relation to variations in winter temperature and winter-annual precipitation (Fig. 2a; Fig. 3b, d, and 3g). The MTCO reconstructed at site SU81-18 oscillates around 0 °C, with values below the freezing point potentially constituting ecological stress for the vegetation. More importantly, the temperature variations are concomitant with large winter and annual precipitation variations, with amplitudes of about 600 and 200 mm for Pann and Pdjf, respectively (Figs. 3g and 10). The smoothed records highlight two phases of high precipitation, between 24 and 22.5 ka and from 21.5 to 19.5 ka. In the Alboran Sea (Fig. 11), the amplitude of variations is generally smaller than that estimated from core SU81-18. However, there is a drop of the same magnitude around 21.5 - 22 ka in both records.

Several studies have reported two main phases of glacier advance in the European Alps during the LGM, with a first phase between 24 and 22 ka and a second phase between 21 and 19 ka (e.g., Ivy-Ochs, 2015; Ivy-Ochs et al., 2018; Kamleitner et al., 2022; Roattino et al., 2023). Since the increase in annual and winter precipitation recorded at the two Iberian sites is concomitant with these glacier advances, we may hypothesize that they are both the result of enhanced regional advection of moisture through the westerlies. In contrast, the pronounced decline in precipitation around 22 ka may correspond to regional changes in atmospheric circulation.

Aside from the precipitation drop recorded around 22 ka, a trend of precipitation decrease is observed on the western Iberian Margin facing the Atlantic (core SU81-18), and in the Alboran Sea (ODP Site 976) (Fig. 8). Similarly, high amplitude variations of MTCO (Fig. 11) with several incursions below 0 °C are reconstructed at site SU81-18, whereas MTCO seems to have remained stable in the Alboran Sea during the LGM (Fig. 11). Based on estimated seasonal SSTs from dinocyst and foraminifer data in core SU81-18 and two others located further south, in the Gulf of Cadiz and on the northwestern Morocco margin, Penaud et al. (2011) highlighted a difference between the western and the southern Iberian margin during the LGM. At site SU81-18 (Penaud et al., 2011), SST estimates based on foraminifera (Fig. 3c) display variations of 5 °C during LGM, but up to 10 °C changes between cold (HSs and YD) and warm phases (LGM, B/A, Holocene). At the same site, the dinocyst-based SST reconstructions depict higher amplitude variations during the LGM, with SST peaks as high as during the B/A and SST drops as low as during HS (Fig. 5 of Penaud et al., 2011). Dinocyst-based SSTs at the two other sites located further south suggest LGM conditions as warm as during the Holocene, with very small variations (Fig. 5 of Penaud, 2011), thus leading to the conclusion that a hydrological front was located between 38 and 36°N on the Atlantic Iberian margins (Penaud et al., 2011) during the last glacial period, including the LGM, as also suggested by Voelker et al. (2009).

According to model simulations, the latitudinal position of the NAO did not shift significantly during the LGM, as the jet stream was forced into a stable and meridional position due to the Northern Hemisphere ice sheets (Riviere et al., 2010; Beghin et al., 2016). However, the LGM might have been characterized by acceleration/deceleration or extension/retraction of the southward jet stream (Riviere et al., 2010). We may thus consider that the variations in precipitation we reconstructed represent variations in the strength of the westerly winds during the LGM.

Justino and Peltier (2005) have argued that despite the southern position of the jet stream, positive phases of the NAO were marked by more southerly winds during the LGM. Small-scale shifts of the Atlantic jet stream may explain differences in pollen-based climate estimates between sites SU81-18 and ODP 976, compatible with Rossby-wave breaking west of the Alps (Fig. 1), as suggested by Luetscher et al. (2015) based on speleothem data. Slight variations in the latitudinal position of the jet stream over the Atlantic Iberian margin may have acted in concert with variations in the hydrological front highlighted by Penaud et al. (2011). Hence, following Justino and Peltier (2005), we can hypothesize that increased precipitation at all sites was related to the positive phase of NAO during the LGM, leading to a displacement of the jet stream over the southern Iberian Peninsula (Fig. 1), while negative phases of NAO (Fig. 1) led to shifting the jet stream southeastward, drastically diminishing precipitation over the southwestern Iberian margin, but not the southeastern margin. Other winter-annual precipitation reconstructions over the region may help confirm whether this hypothesis is correct.

Despite the scarcity of data and many uncertainties about the atmospheric circulation pattern over the study region during the LGM, we may assess millennial-scale variations of the North Atlantic atmospheric circulation linked to variations in oceanic conditions, which are independently demonstrated from IRD concentrations in Northeastern Atlantic core DSDP 609 (Bond and Lotti, 1995).

6. Key features and conclusion

The reconstruction of vegetation types and seasonal climate from 28 ka to 10 ka at five sites from southern Europe highlights a coherent regional pattern of vegetation dynamics with pronounced afforestation during the warm Bølling/Allerød and at the beginning of the Holocene and slight forest decline during the Younger Dryas. In contrast, steppe-like vegetation characterized the cold Heinrich Stadials (HS) HS1 and HS2 (Sanchez-Goñi and Harrison, 2010).

Using the latest version of EMPD2, we estimated seasonal climate parameters from pollen sequences, thereby reconciling climatic information from pollen sequences with many model results and with discrepancies relative to other regional proxy data. Hence, most of the changes reconstructed in this study appear tightly linked to winter climate, particularly to winter and annual precipitation, which exhibit coherent regional patterns. Since present-day vegetation in Southern Europe is primarily influenced by winter precipitation, which depends on the latitudinal movements of the westerlies over Europe (Gouveia et al., 2008), we attribute past regional vegetation and related winter precipitation changes to variations in the strength and/or position of the westerlies over the region.

One of the most critical findings in our study is that our pollen-based climatic estimates provide evidence of relatively high winter and annual precipitation during the LGM in all five sequences, notably over

Southern Iberia, in agreement with many model simulation results (e.g., Laîné et al., 2009; Löfverström et al., 2014; Beghin et al., 2016; Löfverström and Lora, 2017; D'Agostino and Lionello, 2020; Kageyama et al., 2021) and some proxy-data (Vegas et al., 2010; Moreno et al., 2012; Schafer et al., 2016). Large amounts of winter-annual precipitation over the study area are attributed to a southward displacement of the jet stream, and thus the westerlies, due to maximum extension of the Northern Hemisphere ice sheets at the time (e.g., Laîné et al., 2009; Löfverström et al., 2014; Beghin et al., 2016; Löfverström and Lora, 2017; D'Agostino and Lionello, 2020; Kageyama et al., 2021).

Despite the general coherence of data about winter-annual precipitation, some regional gradients are noticed. In particular, during the LGM, larger afforestation in the Iberian Peninsula is evidenced at the three westernmost sites, whereas steppe-like vegetation persisted at Monticchio and Xinias, probably due to a very cold climate. We hypothesize that climate was marked by strong west-east temperature gradients related to the influence of the Fennoscandian and Alpine ice sheets, due to the Rossby wave breaking of the jet stream west of the Alps (see also, Luetscher et al., 2015).

High precipitation variability characterized the LGM in the Atlantic margin sequence, which contrasts with lower variations further east, notably the ODP Site 976 located in the Alboran Sea. This may indicate a climatic front somewhere between the two geographic areas, as already suggested by Penaud et al. (2011). Two distinct phases of increased precipitation are distinguished in the two Iberian records: one at 24-22.5 ka and the other at 21.5-19.5 ka. This is not the case at Padul, and chronological uncertainties prevent association with Monticchio or Xinias for this interval. Nevertheless, these two high-precipitation phases correspond to the two main glacier-advance pulses recorded during the LGM in the European Alps (e.g., Ivy-Ochs, 2015; Ivy-Ochs et al., 2018; Kamleitner et al., 2022; Roattino et al., 2023). From this, we hypothesize generally strong westerlies or southerlies over the entire region during the LGM, with episodic arid phases that could relate to significant weakening or latitudinal shift of the jet stream. Additional climatic reconstructions from northern Morocco and from western to eastern Mediterranean regions would provide constraints on the latitudinal zonation of the westerlies and may confirm or refute the hypothesis that jet-stream Rossby wave breaking west of the Alps was a critical path during the LGM.

Author contributions

JZ and AdV designed the study. JZ, AdV and FE elaborated on the methodology and proceeded with the analyses. JZ, AdV, FE, JC, GJ-M and NC-N contributed to interpreting the results and writing the manuscript. All the authors helped refine the manuscript.

Declaration of competing interest

The authors declare that they have no known competing financial interests or personal relationships that could have appeared to influence the work reported in this paper.

Acknowledgments

We acknowledge financial supports from the GEOTOP, funded by the *Fonds de Recherche du Québec – Nature et Technologies* (FRQNT) and the Hominin Dispersal Research Group (HDRG - http://www.hominindispersals.net/), funded by the *Fonds de Recherche Québécois sur la Société et la Culture* (FRQSC). This research also benefited from funding from the Natural Sciences and Engineering Research Council of Canada (NSERC) through a Discovery grant to AdV and through the international program "Processes and impacts of climate change in the North Atlantic Ocean and the Canadian Arctic (ArcTrain), which is a Collaborative Research and training Experience Program (CREATE).

Appendix A. Supplementary data

Supplementary data to this article can be found online at https://doi.org/10.1016/j.quascirev.2026.109906.

Data availability

A link to the data and/or code is provided as part of this submission.

References

Ahn, J., Brook, E.J., 2008. Atmospheric CO2 and climate on millennial time scales during the last glacial period. Science 322 (5898), 83–85.

Allen, J.R., et al., 2000. Weichselian palynostratigraphy, palaeovegetation and palaeoenvironment; the record from Lago Grande di Monticchio, southern Italy. Quat. Int. 73, 91–110.

Allen, J.R., Huntley, B., 2018. Effects of tephra falls on vegetation: a Late-Quaternary record from southern Italy. J. Ecol. 106 (6), 2456–2472.

Andrieu, V., et al., 1993. La fin du dernier Pléniglaciaire dans les Pyrénées (France): données polliniques, isotopiques et radiométriques. Comptes rendus de l'Académie des sciences. Série 2, Mécanique, Physique, Chimie, Sciences de l'univers, Sciences de la Terre 316 (2), 245–250.

Argenio, C., et al., 2021. Reconstructing ocean surface dynamics over the last~25 kyr at "Shackleton Site" IODP-U1385. Palaeogeogr. Palaeoclimatol. Palaeoecol. 579, 110587.

Austin, W.E., Hibbert, F.D., 2012. Tracing time in the ocean: a brief review of chronological constraints (60–8 kyr) on North Atlantic marine event-based stratigraphies. Quat. Sci. Rev. 36, 28–37.

Bar-Matthews, M., et al., 1997. Late Quaternary paleoclimate in the eastern Mediterranean region from stable isotope analysis of speleothems at Soreq Cave, Israel. Quat. Res. 47 (2), 155–168.

Bar-Matthews, M., et al., 1999. The Eastern Mediterranean paleoclimate as a reflection of regional events: Soreq cave, Israel. Earth Planet Sci. Lett. 166 (1-2), 85–95.

Bard, E., et al., 2000. Hydrological impact of Heinrich events in the subtropical northeast Atlantic. Science 289 (5483), 1321–1324.

Bauska, T.K., et al., 2021. Abrupt changes in the global carbon cycle during the last glacial period. Nat. Geosci. 14 (2), 91–96.

Beghin, P., et al., 2016. What drives LGM precipitation over the western Mediterranean? A study focused on the Iberian Peninsula and northern Morocco. Clim. Dyn. 46, 2611–2631.

Blaauw, M., 2010. Methods and code for 'classical'age-modelling of radiocarbon sequences. Quat. Geochronol. 5 (5), 512–518.

Bond, G.C., Lotti, R., 1995. Iceberg discharges into the North Atlantic on millennial time scales during the last glaciation. Science 267 (5200), 1005–1010.

Bottema, S., 1979. Pollen analytical investigations in Thessaly (Greece). Palaeohistoria 19–40.

Brauer, A., et al., 2007. Evidence for last interglacial chronology and environmental change from Southern Europe. Proc. Natl. Acad. Sci. 104 (2), 450–455.

Cacho, I., et al., 2001. Variability of the western Mediterranean Sea surface temperature during the last 25,000 years and its connection with the Northern Hemisphere climatic changes. Paleoceanography 16 (1), 40–52.

Camuera, J., et al., 2018. Orbital-scale environmental and climatic changes recorded in a new~ 200,000-year-long multiproxy sedimentary record from Padul, southern Iberian Peninsula. Quat. Sci. Rev. 198, 91–114.

Camuera, J., et al., 2019. Vegetation and climate changes during the last two glacial-interglacial cycles in the western Mediterranean: a new long pollen record from Padul (southern Iberian Peninsula). Quat. Sci. Rev. 205, 86–105.

Camuera, J., et al., 2021. Chronological control and centennial-scale climatic subdivisions of the Last Glacial Termination in the western Mediterranean region. Quat. Sci. Rev. 255, 106814.

Camuera, J., et al., 2022. Past 200 kyr hydroclimate variability in the western Mediterranean and its connection to the African Humid Periods. Sci. Rep. 12 (1), 9050.

Canals, M., Casamor, J.L., Lastras, G., Monaco, A., Acosta, J., Berné, S., et al., 2004. The role of canyons in strata formation. Oceanography (Wash. D. C.) 17 (4), 80–91.

Cleator, S.F., et al., 2020. A new multivariable benchmark for Last Glacial Maximum climate simulations. Clim. Past 16 (2), 699–712.

CLIMAP Project Members, McIntyre, A., Cline, R., 1981. Seasonal Reconstructions of the Earth's Surface at the Last Glacial Maximum. Geological Society of America.

Combourieu-Nebout, N., et al., 2009. Rapid climatic variability in the west Mediterranean during the last 25 000 years from high resolution pollen data. Clim. Past 5 (3), 503–521.

Combourieu-Nebout, N., Turon, J.L., Zahn, R., Capotondi, L., Londeix, L., Pahnke, K., 2002. Enhanced aridity and atmospheric high-pressure stability over the western Mediterranean during the North Atlantic cold events of the past 50 ky. Geology 30 (10), 863–866.

D'Agostino, R., Lionello, P., 2020. The atmospheric moisture budget in the Mediterranean: mechanisms for seasonal changes in the Last Glacial Maximum and future warming scenario. Quat. Sci. Rev. 241, 106392.

Davis, B.A.S., et al., 2020. The Eurasian Modern Pollen Database (EMPD), version 2. Earth Syst. Sci. Data Discuss. 2020, 1–41.

Davis, B.A.S., et al., 2022. The climate and vegetation of Europe, North Africa and the Middle East during the Last Glacial Maximum (21,000 years BP) based on pollen data. Clim. Past Discuss 1–66.

de Abreu, L., et al., 2003. Millennial-scale oceanic climate variability off the Western Iberian margin during the last two glacial periods. Mar. Geol. 196 (1-2), 1–20.

de Vernal, A., et al., 2005. Reconstruction of sea-surface conditions at middle to high latitudes of the Northern Hemisphere during the Last Glacial Maximum (LGM) based on dinoflagellate cyst assemblages. Quat. Sci. Rev. 24 (7-9), 897–924.

Del Gobbo, C., et al., 2022. Atmosphere-cryosphere interactions at 21 ka BP in the European Alps. Clim. Past Discuss 1–24.

Dyke, A.S., et al., 2002. The Laurentide and Innuitian ice sheets during the last glacial maximum. Quat. Sci. Rev. 21 (1-3), 9–31.

Ehlers, J., Gibbard, P.L., 2004. Quaternary glaciations-extent and Chronology: Part I: Europe. Elsevier.

El Amrani, M., et al., 2008. Contrasted morphosedimentary activity of the lower Kert River (northeastern Morocco) during the Late Pleistocene and the Holocene. Possible impact of bioclimatic variations and human action. C. R. Geosci. 340 (8), 533–542.

Elenga, H., et al., 2000. Pollen-based biome reconstruction for southern Europe and Africa 18,000 yr BP. J. Biogeogr. 27 (3), 621–634.

Eynaud, F., et al., 2009. Position of the Polar Front along the western Iberian margin during key cold episodes of the last 45 ka. G-cubed 10 (7).

Eynaud, F., et al., 2018. Compiling multiproxy quantitative hydrographic data from Holocene marine archives in the North Atlantic: a way to decipher oceanic and climatic dynamics and natural modes? Global Planet. Change 170, 48–61.

Eynaud, F., et al., 2021. Are past sea-ice reconstructions based on planktonic Foraminifera realistic? Study of the last 50 ka as a test to validate reconstructed paleohydrography derived from transfer functions applied to their fossil assemblages. Geosciences 11 (10), 409.

Fabres, J., et al., 2002. Composition and spatio-temporal variability of particle fluxes in the Western Alboran Gyre, Mediterranean Sea. J. Mar. Syst. 33, 431–456.

Fick, S.E., Hijmans, R.J., 2017. WorldClim 2: new 1-km spatial resolution climate surfaces for global land areas. Int. J. Climatol. 37 (12), 4302–4315.

Fletcher, W.J., et al., 2010. Millennial-scale variability during the last glacial in vegetation records from Europe. Quat. Sci. Rev. 29 (21-22), 2839–2864.

Fletcher, W.J., Sánchez-Goñi, M.F., 2008. Orbital-and sub-orbital-scale climate impacts on vegetation of the western Mediterranean basin over the last 48,000 yr. Quat. Res. 70 (3), 451–464.

García-Amorena, I., et al., 2007. The Late Quaternary coastal forests of western Iberia: a study of their macroremains. Palaeogeogr. Palaeoclimatol. Palaeoecol. 254 (3-4), 448–461.

Genty, D., et al., 2010. Isotopic characterization of rapid climatic events during OIS3 and OIS4 in Villars Cave stalagmites (SW-France) and correlation with Atlantic and Mediterranean pollen records. Quat. Sci. Rev. 29 (19-20), 2799–2820.

Giraudi, C., 2017. Climate evolution and forcing during the last 40 ka from the oscillations in apennine glaciers and high mountain lakes, Italy. J. Quat. Sci. 32 (8), 1085–1098.

González-Sampériz, P., et al., 2006. Climate variability in the Spanish Pyrenees during the last 30,000 yr revealed by the El Portalet sequence. Quat. Res. 66 (1), 38–52.

Gouveia, C., et al., 2008. The North Atlantic oscillation and European vegetation dynamics. Int. J. Climatol.: A Journal of the Royal Meteorological Society 28 (14), 1835–1847.

Guiot, J., 1990. Methodology of the last climatic cycle reconstruction in France from pollen data. Palaeogeogr. Palaeoclimatol. Palaeoecol. 80 (1), 49–69.

Guiot, J., et al., 2000. Inverse vegetation modeling by Monte Carlo sampling to reconstruct palaeoclimates under changed precipitation seasonality and CO2 conditions: application to glacial climate in Mediterranean region. Ecol. Model. 127 (2-3), 119–140.

Harrison, S.P., Prentice, C.I., 2003. Climate and CO2 controls on global vegetation distribution at the last glacial maximum: analysis based on palaeovegetation data, biome modelling and palaeoclimate simulations. Glob. Change Biol. 9 (7), 983–1004.

Hurrell, J.W., 1995. Decadal trends in the North Atlantic Oscillation: regional temperatures and precipitation. Science 269 (5224), 676–679.

Hurrell, J.W., et al., 2003. An overview of the North Atlantic oscillation. Geophysical Monograph-American Geophysical Union 134, 1–36.

Ivy-Ochs, S., 2015. Glacier variations in the European Alps at the end of the last glaciation. Cuadernos de investigación geográfica: Geographical Research Letters (41), 295–315.

Ivy-Ochs, S., et al., 2018. New geomorphological and chronological constraints for glacial deposits in the Rivoli-Avigliana end-moraine system and the lower Susa Valley (Western Alps, NW Italy). J. Quat. Sci. 33 (5), 550–562.

Jackson, S.T., Overpeck, J.T., 2000. Responses of plant populations and communities to environmental changes of the late Quaternary. Paleobiology 26 (S4), 194–220.

Justino, F., Peltier, W.R., 2005. The glacial North Atlantic Oscillation. Geophys. Res. Lett. 32 (21).

Kageyama, M., et al., 1999. Northern Hemisphere storm tracks in present day and last glacial maximum climate simulations: a comparison of the European PMIP models. J. Clim. 12 (3), 742–760.

Kageyama, M., Laîné, A., Abe-Ouchi, A., Braconnot, P., Cortijo, E., Crucifix, M., et al., 2006. Last Glacial Maximum temperatures over the North Atlantic, Europe and western Siberia: a comparison between PMIP models, MARGO sea–surface temperatures and pollen-based reconstructions. Quat. Sci. Rev. 25 (17-18), 2082–2102.

Kageyama, M., et al., 2017. The PMIP4 contribution to CMIP6–Part 4: scientific objectives and experimental design of the PMIP4-CMIP6 last Glacial Maximum experiments and PMIP4 sensitivity experiments. Geosci. Model Dev. (GMD) 10 (11), 4035–4055.

Kageyama, M., et al., 2021. The PMIP4 last Glacial Maximum experiments: preliminary results and comparison with the PMIP3 simulations. Clim. Past 17 (3), 1065–1089.

Kamleitner, S., et al., 2022. The ticino-toce glacier system (Swiss-Italian Alps) in the framework of the alpine last glacial maximum. Quat. Sci. Rev. 279, 107400.

La Violette, P.E., 1986. Short-term measurements of surface currents associated with the Alboran Sea Gyre during Donde Va? J. Phys. Oceanogr. 16 (2), 262–279.

Laîné, A., et al., 2009. Northern hemisphere storm tracks during the last glacial maximum in the PMIP2 ocean-atmosphere coupled models: energetic study, seasonal cycle, precipitation. Clim. Dyn. 32 (5), 593–614.

Lambeck, K., et al., 2006. Constraints on the Late Saalian to early Middle Weichselian ice sheet of Eurasia from field data and rebound modelling. Boreas 35 (3), 539–575.

Lambeck, K., et al., 2014. Sea level and global ice volumes from the Last Glacial Maximum to the Holocene. Proc. Natl. Acad. Sci. 111 (43), 15296–15303.

Langgut, D., et al., 2011. Vegetation and climate changes in the South Eastern Mediterranean during the Last Glacial-Interglacial cycle (86 ka): new marine pollen record. Quat. Sci. Rev. 30 (27-28), 3960–3972.

Lécuyer, C., et al., 2021. Temperature and precipitation regime in LGM human refugia of southwestern Europe inferred from δ13C and δ18O of large mammal remains. Quat. Sci. Rev. 255, 106796.

Lézine, A.M., Denèfle, M., 1997. Enhanced anticyclonic circulation in the eastern North Atlantic during cold intervals of the last deglaciation inferred from deep-sea pollen records. Geology 25 (2), 119–122.

Lisiecki, L.E., Raymo, M.E., 2005. A Pliocene-Pleistocene stack of 57 globally distributed benthic δ18O records. Paleoceanography 20 (1).

Löfverström, M., et al., 2014. Evolution of the large-scale atmospheric circulation in response to changing ice sheets over the last glacial cycle. Clim. Past 10 (4), 1453–1471.

Löfverström, M., Lora, J.M., 2017. Abrupt regime shifts in the North Atlantic atmospheric circulation over the last deglaciation. Geophys. Res. Lett. 44 (15), 8047–8055.

Lofverstrom, M., 2020. A dynamic link between high-intensity precipitation events in southwestern North America and Europe at the Last Glacial Maximum. Earth Planet Sci. Lett. 534, 116081.

Luetscher, M., et al., 2015. North Atlantic storm track changes during the Last Glacial Maximum recorded by Alpine speleothems. Nat. Commun. 6 (1), 6344.

Magri, D., Parra, I., 2002. Late Quaternary western Mediterranean pollen records and African winds. Earth Planet Sci. Lett. 200 (3-4), 401–408.

Magyari, E.K., et al., 2014a. Late Pleniglacial vegetation in eastern-central Europe: are there modern analogues in Siberia? Quat. Sci. Rev. 95, 60–79.

Magyari, E.K., et al., 2014b. Vegetation and environmental responses to climate forcing during the Last Glacial Maximum and deglaciation in the East Carpathians: attenuated response to maximum cooling and increased biomass burning. Quat. Sci. Rev. 106, 278–298.

MARGO Project Members, 2009. Constraints on the magnitude and patterns of ocean cooling at the Last Glacial Maximum. Nat. Geosci. 2, 127–132.

Martrat, B., et al., 2014. Similarities and dissimilarities between the last two deglaciations and interglaciations in the North Atlantic region. Quat. Sci. Rev. 99, 122–134.

Mix, A.C., et al., 2001. Environmental processes of the ice age: land, oceans, glaciers (EPILOG). Quat. Sci. Rev. 20 (4), 627–657.

Moreno, A., et al., 2012. Northern Iberian abrupt climate change dynamics during the last glacial cycle: a view from lacustrine sediments. Quat. Sci. Rev. 36, 139–153.

Naughton, F., et al., 2007. Present-day and past (last 25 000 years) marine pollen signal off western Iberia. Mar. Micropaleontol. 62 (2), 91–114.

North Greenland Ice Core Project members, 2004. High-resolution record of Northern Hemisphere climate extending into the last interglacial period. Nature 431 (7005), 147–151.

Overpeck, J.T., et al., 1985. Quantitative interpretation of fossil pollen spectra: dissimilarity coefficients and the method of modern analogs. Quat. Res. 23 (1), 87–108.

Pascual, A., et al., 2020. Palaeoceanographic and palaeoclimatic changes during the last 37,000 years detected in the SE Bay of Biscay based on benthic foraminifera. Quat. Int. 566, 323–336.

Penaud, A., et al., 2011. Hydrological processes affecting the subtropical NE Atlantic (34-38° N) over the last 30 ka: evidence from phyto-and zooplankton assemblages. Biogeosci. Discuss. 8 (2), 2281–2327.

Peyron, O., et al., 1998. Climatic reconstruction in Europe for 18,000 yr BP from pollen data. Quat. Res. 49 (2), 183–196.

Pinto, J.G., Ludwig, P., 2020. Extratropical cyclones over the North Atlantic and western Europe during the Last Glacial Maximum and implications for proxy interpretation. Clim. Past 16 (2), 611–626.

Prentice, I.C., et al., 1992a. Mediterranean vegetation, lake levels and palaeoclimate at the Last Glacial Maximum. Nature 360 (6405), 658–660.

Prentice, I.C., et al., 1992. Special paper: a global biome model based on plant physiology and dominance, soil properties and climate. J. Biogeogr. 117–134.

Prentice, C., et al., 1996. Reconstructing biomes from palaeoecological data: a general method and its application to European pollen data at 0 and 6 ka. Clim. Dyn. 12, 185–194.

Prentice, I.C., et al., 2017. Reconstructing ice-age palaeoclimates: quantifying low-CO2 effects on plants. Global Planet. Change 149, 166–176.

Prentice, I.C., et al., 2022. Accounting for atmospheric carbon dioxide variations in pollen-based reconstruction of past hydroclimates. Global Planet. Change 211, 103790.

Ramstein, G., et al., 2007. How cold was Europe at the Last Glacial Maximum? A synthesis of the progress achieved since the first PMIP model-data comparison. Clim. Past 3 (2), 331–339.

Rasmussen, S.O., et al., 2014. A stratigraphic framework for abrupt climatic changes during the Last Glacial period based on three synchronized Greenland ice-core records: refining and extending the INTIMATE event stratigraphy. Quat. Sci. Rev. 106, 14–28.

Reille, M., Andrieu, V., 1995. The late Pleistocene and Holocene in the Lourdes Basin, Western Pyrénées, France: new pollen analytical and chronological data. Veg. Hist. Archaeobotany 4, 1–21.

Reimer, P.J., et al., 2013. IntCal13 and Marine13 radiocarbon age calibration curves 0–50,000 years cal BP. Radiocarbon 55 (4), 1869–1887.

Ribolini, A., et al., 2022. Last glacial maximum and early deglaciation in the stura valley, southwestern European Alps. Quat. Sci. Rev. 295, 107770.

Ríos, A.F., et al., 1992. Water masses in the upper and middle North Atlantic Ocean east of the Azores. Deep-Sea Res., Part A 39 (3-4), 645–658.

Riviere, G., et al., 2010. Links between Rossby wave breaking and the North Atlantic Oscillation–Arctic Oscillation in present-day and Last Glacial Maximum climate simulations. J. Clim. 23 (11), 2987–3008.

Roattino, T., et al., 2023. Paleogeographical reconstruction of the western French Alps foreland during the last glacial maximum using cosmogenic exposure dating. Quat. Res. 111, 68–83.

Rochon, A., Vernal, A.D., 1994. Palynomorph distribution in recent sediments from the Labrador Sea. Canadian Journal of Earth Sciences 31 (1), 115–127.

Rodrigo-Gámiz, M., et al., 2022. Paleoclimate reconstruction of the last 36 kyr based on branched glycerol dialkyl glycerol tetraethers in the Padul palaeolake record (Sierra Nevada, southern Iberian Peninsula). Quat. Sci. Rev. 281, 107434.

Rodrıguez, S., et al., 2001. Saharan dust contributions to PM10 and TSP levels in Southern and Eastern Spain. Atmos. Environ. 35 (14), 2433–2447.

Rodwell, M.J., Hoskins, B.J., 2001. Subtropical anticyclones and summer monsoons. J. Clim. 14 (15), 3192–3211.

Roucoux, K.H., et al., 2005. The response of NW Iberian vegetation to North Atlantic climate oscillations during the last 65 kyr. Quat. Sci. Rev. 24 (14-15), 1637–1653.

Sánchez Goñi, M.F., et al., 2008. Contrasting impacts of Dansgaard–Oeschger events over a western European latitudinal transect modulated by orbital parameters. Quat. Sci. Rev. 27 (11-12), 1136–1151.

Sánchez Goñi, Desprat, S., Fletcher, W.J., Morales-Molino, C., Naughton, F., Oliveira, D., Zorzi, C., 2018. Pollen from the deep-sea: A breakthrough in the mystery of the Ice Ages. Frontiers in plant science 9, 38.

Sánchez Goñi, M.F., Harrison, S.P., 2010. Millennial-scale climate variability and vegetation changes during the Last Glacial: concepts and terminology. Quat. Sci. Rev. 29 (21-22), 2823–2827.

Sánchez Goñi, Landais, A., Cacho, I., Duprat, J., Rossignol, L., 2009. Contrasting intrainterstadial climatic evolution between high and middle North Atlantic latitudes: a close-up of Greenland. Interstadials 8 and 12. Geochemistry, Geophysics, Geosystems 10 (4).

Sánchez-Goñi, M.F., et al., 2002. Synchroneity between marine and terrestrial responses to millennial scale climatic variability during the last glacial period in the Mediterranean region. Clim. Dyn. 19, 95–105.

Sánchez-Goñi, M.F., et al., 2017. The ACER pollen and charcoal database: a global resource to document vegetation and fire response to abrupt climate changes during the last glacial period. Earth Syst. Sci. Data Discuss. 2017, 1–33.

Schäfer, I.K., et al., 2016. Evidence for humid conditions during the last glacial from leaf wax patterns in the loess–paleosol sequence El Paraíso, Central Spain. Quat. Int. 407, 64–73.

Shao, Y., et al., 2018. Statistical reconstruction of global vegetation for the last glacial maximum. Global Planet. Change 168, 67–77.

Shields, C.A., et al., 2019. Meridional heat transport during atmospheric rivers in high-resolution CESM climate projections. Geophys. Res. Lett. 46 (24), 14702–14712.

Skinner, C.B., et al., 2023. Atmospheric river contributions to ice sheet hydroclimate at the last glacial maximum. Geophys. Res. Lett. 50 (1) e2022GL101750.

Šmilauer, P., Lepš, J., 2014. Multivariate Analysis of Ecological Data Using CANOCO 5. Cambridge university press.

Spötl, C., et al., 2021. Increased autumn and winter precipitation during the Last Glacial Maximum in the European Alps. Nat. Commun. 12 (1), 1839.

Svendsen, J.I., et al., 2004. Late Quaternary ice sheet history of northern Eurasia. Quat. Sci. Rev. 23 (11-13), 1229–1271.

Tarasov, L., et al., 2012. A data-calibrated distribution of deglacial chronologies for the North American ice complex from glaciological modeling. Earth Planet Sci. Lett. 315, 30–40.

Toucanne, S., et al., 2015. Millennial-scale fluctuations of the European Ice Sheet at the end of the last glacial, and their potential impact on global climate. Quat. Sci. Rev. 123, 113–133.

Turon, J.L., 1984. Direct land/sea correlations in the last interglacial complex. Nature 309 (5970), 673–676.

Turon, J.L., et al., 2003. Land–sea correlations for the last glaciation inferred from a pollen and dinocyst record from the Portuguese margin. Quat. Res. 59 (1), 88–96.

Tzedakis, P.C., et al., 2004. Ecological thresholds and patterns of millennial-scale climate variability: the response of vegetation in Greece during the last glacial period. Geology 32 (2), 109–112.

Valero-Garcés, B.L., et al., 2004. Paleohydrological fluctuations and steppe vegetation during the last glacial maximum in the central Ebro valley (NE Spain). Quat. Int. 122 (1), 43–55.

Vegas, J., et al., 2010. Identification of arid phases during the last 50 cal. ka BP from the Fuentillejo maar-lacustrine record (Campo de Calatrava Volcanic Field, Spain). J. Quat. Sci. 25 (7), 1051–1062.

Voelker, A.H.L., et al., 2009. Hydrographic conditions along the western Iberian margin during marine isotope stage 2. G-cubed 10 (12).

Watts, W.A., et al., 1996a. Vegetation history and palaeoclimate of the last glacial period at Lago Grande di Monticchio, southern Italy. Quat. Sci. Rev. 15 (2-3), 133–153.

Watts, W.A., et al., 1996b. Vegetation history and climate of the last 15,000 years at Laghi di Monticchio, southern Italy. Quat. Sci. Rev. 15 (2-3), 113–132.

Watts, W.A., et al., 2000. Palaeoecology of three interstadial events during oxygen-isotope Stages 3 and 4: a lacustrine record from Lago Grande di Monticchio, southern Italy. Palaeogeogr. Palaeoclimatol. Palaeoecol. 155 (1-2), 83–93.

Wulf, S., et al., 2004. Tephrochronology of the 100 ka lacustrine sediment record of Lago Grande di Monticchio (southern Italy). Quat. Int. 122 (1), 7–30.

Zaragosi, S., et al., 2001. Initiation of the European deglaciation as recorded in the northwestern Bay of Biscay slope environments (Meriadzek Terrace and Trevelyan Escarpment): a multi-proxy approach. Earth Planet Sci. Lett. 188 (3-4), 493–507.

Zaragosi, S., et al., 2006. The impact of the last European deglaciation on the deep-sea turbidite systems of the Celtic-Armorican margin (Bay of Biscay). Geo Mar. Lett. 26, 317–329.

Zolitschka, B., Negendank, J.F., 1996. Sedimentology, dating and palaeoclimatic interpretation of a 76.3 ka record from Lago Grande di Monticchio, southern Italy. Quat. Sci. Rev. 15 (2-3), 101–112.

Zumaque, J., et al., 2025a. A ready-to-use version of the Eurasian Modern Pollen Database 2 (EMPD 2; Davis et al., 2020) for paleoclimatic reconstructions. Data Brief, 111657.

Zumaque, J., et al., 2025b. Ready-to-use version of the Eurasian Modern Pollen Database version 2, with 90 pollen taxa and 7634 sites. PANGAEA. https://doi.org/10.1594/PANGAEA.973997.

Zumaque, J., et al., 2025c. Decoupled winter and summer climate changes in southern Europe during the Dansgaard-Oeschger cycles. Quat. Sci. Rev. 359, 109273.

Eynaud, F., Rossignol, L., & Gasparotto, M. C. (2013). Planktic foraminifera throughout the Pleistocene: From cell to populations to past marine hydrology.

de Vernal, A., Radi, T., Zaragosi, S., Van Nieuwenhove, N., Rochon, A., Allan, E., . & Richerol, T. (2020). Distribution of common modern dinoflagellate cyst taxa in surface sediments of the Northern Hemisphere in relation to environmental parameters: The new n= 1968 database. *Marine Micropaleontology*, *159*, 101796.